

Abstract

New functional coatings for optical applications have an increasing complexity in their microstructure. TiO₂-SiO₂ coatings are being produced with tilted, zig-zaged, and curled columns in order to achieve different optical properties. However, the mechanical properties of these coatings and the influence of the different microstructural features are not known. Mechanical properties are key parameter to assure the structural integrity and reliability of the components.

In this project, the evaluation of the mechanical properties and the damage mechanisms in terms of different growth structure (tilted, zig-zaged or spiral) and growth angle (70° or 85°) has been studied.

To accomplish it, mechanical characterization at micro- and nanometric length scale by means of nanoindentation and nanoscratch tests have been made. The superficial damage induced using a sharp indenter was studied by using confocal laser scanning microscopy, atomic force microscopy and field emission scanning electron microscopy. Moreover, the sub-superficial damage as well as the adhesive and/or cohesive failure between coating and substrate was studied by focused ion beam.

Results show that the main parameter controlling the mechanical response is the glancing angle. Coating architecture and number of layers have only a minor effect on the mechanical response. Low angle coatings present higher resistance to scratch testing than high angle coatings, but they show a brittle failure behavior.

SUMMARY

ABSTRACT	1
SUMMARY	2
1. ACRONYMS	5
2. PREFACE	7
2.1. Thesis origin	7
2.2. Previous requirements.....	7
3. INTRODUCTION	9
3.1. Properties of TiO ₂ -SiO ₂ coatings	9
3.2. Deposition techniques	9
3.2.1. Oblique Angle Deposition, OAD.....	10
3.2.2. Glancing Angle Deposition GLAD	12
4. MECHANICAL PROPERTIES	14
4.1. Tip geometries.....	15
4.2. Continuous stiffness measurements, CSM	16
4.3. Contact Mechanisms	17
4.3.1. Elastic contact.....	17
4.3.2. Elasto-plastic contact	18
4.4. Mechanical properties determination on coating systems.....	20
4.5. Tribological characterization of coatings.....	23
5. STATE OF THE ART	25
6. OBJECTIVES	26
7. EXPERIMENTAL PROCEDURE	27
7.1. Samples Preparation	27
7.2. Mechanical characterization	30
7.3. Superficial observation	33
7.3.1. Laser Scanning Confocal Microscopy, LSCM.....	33
7.3.2. Field Emission Scanning Electron Microscopy, FESEM	34
7.3.3. Atomic Force Microscopy, AFM	35
7.4. Sub-Superficial observation.....	36
8. RESULTS AND DISCUSSION	39
8.1. Mechanical Characterization	39

8.1.1. Hardness.....	39
8.1.2. Elastic modulus	46
8.1.3. Indentation stress-strain curve	53
8.1.4. Mechanical properties vs Microstructural properties	55
8.2. Fracture Events.....	58
8.2.1. Chipping and pile-up damage effect.....	58
8.2.2. Decohesion or interfacial cracking.....	60
8.2.3. Fracture events induce under sliding contact	62
8.3. Sub-superficial observation	65
8.4. Tribological characterization	70
9. CONCLUSIONS	72
10. FUTURE WORK	73
11. ENVIRONMENTAL IMPACT	74
12. ECONOMICAL STUDY	75
13. ACKNOWLEDGMENTS	76
REFERENCES	77

1. Acronyms

a: Contact indentation radius

a/R: Indentation strain

AFM: Atomic force microscopy

CSM: Continuous stiffness measurement

CVD: Chemical vapor deposition

E: Elastic modulus

E_c: Coating elastic modulus

E_{eff}: Effective elastic modulus

F: Vapor flux

F_∥: Vapor flux projected parallel to the substrate

F_⊥: Vapor flux projected perpendicular to the substrate

FESEM: Field emission scanning electron microscopy

FIB/FESEM: Focused ion beam / Field emission scanning electron microscopy

GLAD: Glancing angle deposition

GPa: Gigapascal

H: Hardness

h: Penetration depth or displacement into the surface

h/t: Penetration depth/thickness

H_c: Coating hardness

h_a: Displacement induced

h_e: Elastic penetration depth

h_f: Final penetration depth

h_{max}: Maximum penetration depth

h_t: Total displacement into the sample

Hz: Hertz

IIT: Instrumented indentation technique

keV: Kiloelectron-volt

kV: Kilovolt

kWh_e: Electrical kilowatt per hour

L_{cr}: Critical length

LSCM: Laser scanning confocal microscopy

mN: Milinewton

nm: Nanometer

OAD: Oblique angle deposition

P: Applied load

Pa: Pascal

pA: Picoampere

P_{cr} : Critical load
 p_m : Mean contact pressure or indentation stress
 P_{max} : Maximum applied load
PVD: Physical vapor deposition
R: Tip radius
S: Elastic unloading stiffness or Stiffness
SEM: Scanning electron microscopy
SiO₂: Silicon oxide
t: Thickness
TiO₂: Titanium oxide
V: Volt
 β : growing angle
 ϵ : Strain
 θ : Incident angle
 λ : Bilayer period
 μm : Micrometer
 ν : Poisson's ratio
 σ : Stress

2. Preface

2.1. Thesis origin

Study of the mechanical integrity of the new structural designed optical coatings TiO₂-SiO₂ supplied by the “*Instituto de Ciencia de los Materiales de Sevilla*”, “CSIC-Sevilla”, whose optical properties are known either its relationship with the coating growing structure, but its mechanical integrity as a function of their microstructure are not known.

2.2. Previous requirements

Nanoindentation and nanoscratch international standards:

- **ISO 14577-1:2002**, Metallic materials, Instrumented indentation test for hardness and materials parameters. Part 1: Test method.
- **ISO 14577-2:2002**, Metallic materials, Instrumented indentation test for hardness and materials parameters. Part 2: Verification and calibration of testing machines.
- **ISO 14577-3:2002**, Metallic materials, Instrumented indentation test for hardness and materials parameters. Part 3: Calibration of reference blocks.
- **ISO 14577-4:2002**, Metallic materials, Instrumented indentation test for hardness and materials parameters. Part 4: Test method for metallic and non-metallic coatings.
- **ASTM C-1624-05**, Standard Test Method for Adhesion Strength and Mechanical Failure Modes of Ceramic Coatings by Quantitative Single Point Scratch Testing.

3. Introduction

3.1. Properties of TiO₂-SiO₂ coatings

TiO₂-SiO₂ coatings are commonly used as self-cleaning coatings above porous carbonate substrates, due its hydrophobic properties, in which they increase significantly the substrate's mechanical properties, around 20% increase in hardness [1,2].

The properties of the coatings are related to the deposition technique used as will be comment in further sections. For a bulk TiO₂-SiO₂ coating the standard hardness values are rounding 2 GPa [1,2]. However, for new structure coated specimens (zig-zaged TiO₂-SiO₂), the hardness decreases until 0.5 GPa as reported elsewhere [3,4].

3.2. Deposition techniques

Mainly, the deposition techniques can be classified in two different groups: (i) Physical vapor deposition, PVD and (ii) Chemical vapor deposition, CVD. The main difference between both techniques is the raw material used in each deposition technique [6]. In PVD the material that is going to be deposited starts in a solid state, whereas in CVD it should be introduced in the reaction chamber as a gas.

Both deposition techniques can be divided in four elementary steps [6]:

i) Evaporation: this step is exclusively used in PVD, and its target is to give enough energy to the material that is going to be deposited in order to vaporize the atoms of the surface. The energy source can be either thermal or an electron/ion beam.

ii) Transportation: this process only consists on the movement of the gas atoms (either vaporized in PVD or injected in CVD) from the source to the substrate to be coated. This trajectory can be straight line or curved.

iii) Reaction: if the coating is a metal based (i.e. metal oxide, metal nitride or metal carbide), its atoms will react with the corresponding gas (oxygen, nitrogen, methane, etc.) during the transport stage. If no reaction is needed, the atmosphere of the reaction chamber should be inert being N₂ the main inert gas used.

iv) Deposition: during this step, the coating is build up on the substrate surface.

It is well known that the widely employed deposited technique is the PVD instead of the CVD technique, a schematic representation of the PVD technique is shown in **Figure 3.1**:

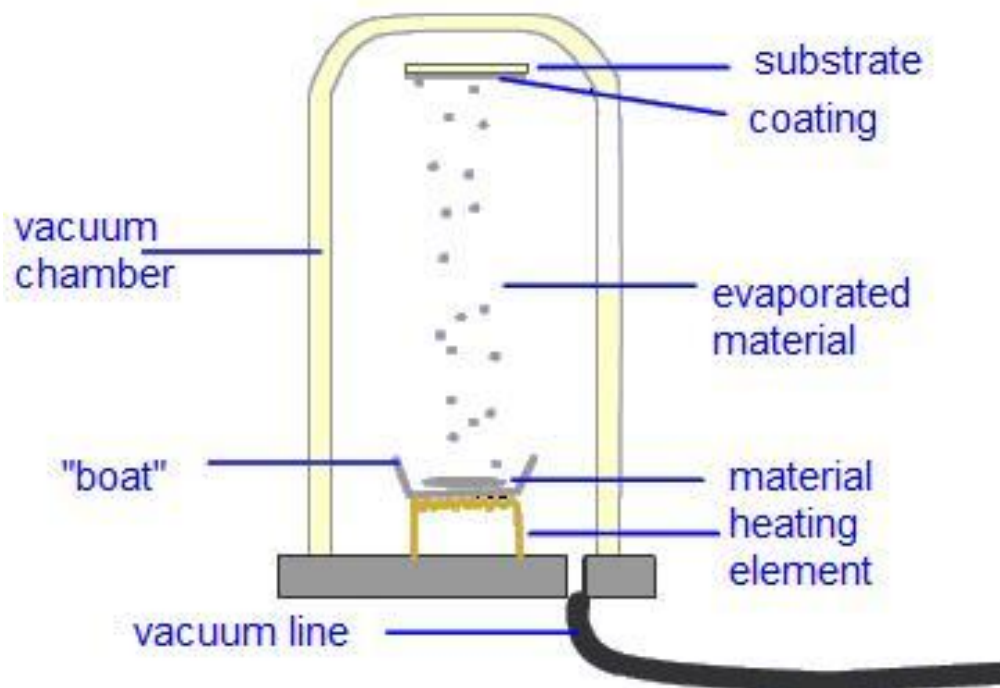


Figure 3.1.- Schematic representation of PVD setup. Extracted from [5].

Furthermore, inside of each deposition group, exist plenty of deposition techniques and they are going to be briefly reviewed below:

3.2.1. Oblique Angle Deposition, OAD

Oblique angle deposition (OAD) is a physic vapor deposition technique; it was one of the first methods that allowed having a tilted coating as reported in [6].

Its experimental setup is simple, as it can be appreciated in **Figure 3.2a**. The deposition source has an angle θ with respect to the normal substrate surface, where the vapor flux (F) can be projected as the same direction as the normal substrate direction (F_{\perp}) or parallel to this (F_{\parallel}), where it can be determined as follows [6]:

$$F_{\perp} = F \cos \theta \quad \text{Equation 3.1}$$

$$F_{\parallel} = |F \sin \theta| \quad \text{Equation 3.2}$$

This decomposition of flux creates the shadowing effect which is that all the tallest columns will receive more atoms as compared to the shortest ones, making them grow and keeping the others small.

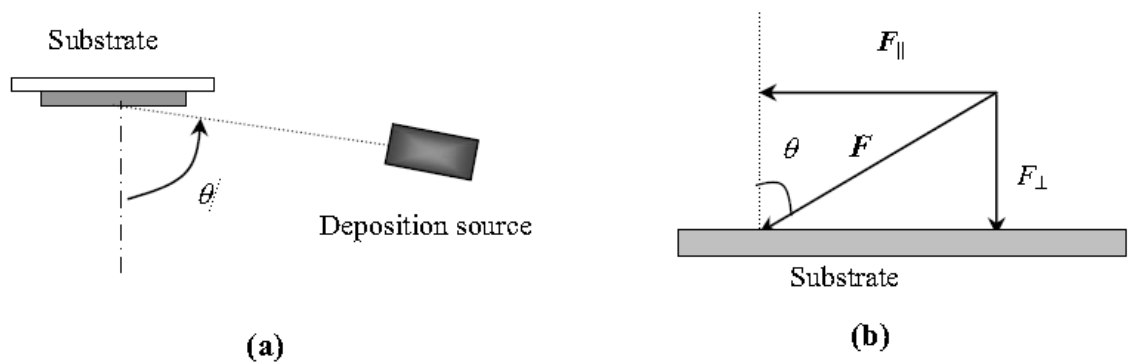


Figure 3.2.- a) Scheme of the setup and **b)** decomposition of vapor flux [6].

During the deposition process, initially the vaporized atoms will randomly form islands on the substrate. Then, the initial nucleated islands act as shadowing centers. This process leaves the tallest islands grow into columns, and a nanocolumnar film will be formed. The lateral component F_{\parallel} is the reason of the shadowing effect as it depicted in **Figure 3.3**. So, if F_{\parallel} remains constant during the deposition, a columnar film with tilt angle (β) not related with θ , will be formed.

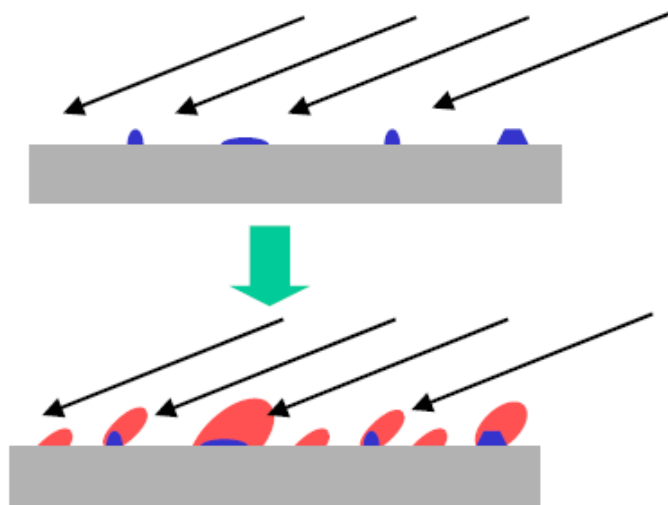


Figure 3.3.- Shadowing effect generated during the deposition process [6].

The coatings deposited using this technique presents some remarkable characteristics: i.e. porous nanocolumnar structure, tilted structures out from the surface normal yielding a great anisotropy in the deposited layer, among others.

3.2.2. Glancing Angle Deposition GLAD

Glancing angle deposition (GLAD) is based in OAD [6] process, as its setup is basically the same, with the only difference that the substrate can be moved by two different motors. One of them controls the incident angle (θ) and the other one controls the rotation movement allowing the substrate to be rotated by its center.

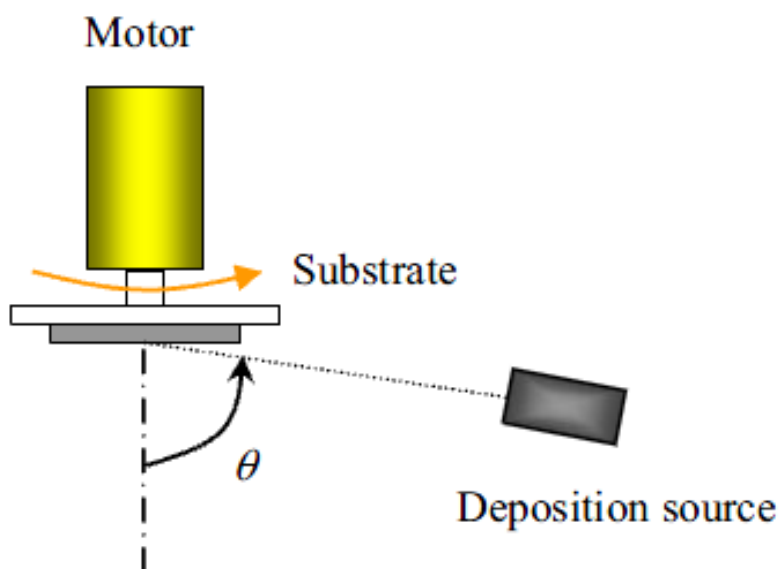


Figure 3.4.- Schematic representation of GLAD setup [2].

With this two movements being controlled by a computer, the nanocolumns created during the deposition process can be sculptured in many different shapes, as: compact, spiral, zig-zag, helical or vertical shape among others.

This deposition process presents several **advantages** among the other deposition techniques, such as:

- (i) It can form vertical aligned nanorod array easily, whereas in most of traditional CVD or PVD lots of efforts have to be made to forms aligned nanowires,
- (ii) any material that can be evaporated can be used in this process, and
- (iii) the size (with a variable diameter that can oscillate between 40 to 70nm) and density of nanocolumns can be controlled by the vapor incident angle, θ .

As commented previously, the mechanical integrity of these optical coatings is unknown. As the coating of interest present a roughly homogeneous thickness of $\approx 1-2 \mu\text{m}$, it is necessary to use a technique which helps to determine the mechanical properties at micro- and

nanometric length scale. In order to study the mechanical integrity of these coatings, the following considerations have to be taken into account:

- (i) they are ceramic oxides, they will have a brittle fracture,
- (ii) as their length is in the nanometric scale, macro- or micromechanical characterization, such as Vickers testing or Charpy testing, cannot be performed and
- (iii) as the properties for the coating layer are unknown and its thickness is around of several micrometers ($\sim 2 \mu\text{m}$), micro- and nanomechanical characterization techniques are needed to study their mechanical integrity in terms of hardness and elastic modulus using the instrumented indentation technique.

In order to know the mechanical properties of this coatings macromechanical tests are not useful, due they induce massive damage so fast than the superficial properties cannot be recorded. That is why micro- and nanomechanical technique were developed. In the following section, the main principles for the instrumented indentation technique as well as different considerations in order to assure the mechanical properties for the coatings of study is going to be reviewed in detail.

4. Mechanical properties

As described previously, it is necessary to better understand how the coating structure can modify the mechanical response into the elastic and elasto-plastic range using different tip geometries as well as the fracture mechanisms activated under different contact modes (uniaxial compression and/or sliding).

In this sense, nanoindentation (also known as instrumented indentation technique (IIT)) provides the necessary resolution to probe the mechanical properties of the $\text{TiO}_2\text{-SiO}_2$ coatings with different structures.

Nanoindentation technique allows to determine hardness (H) and elastic modulus (E) at the same time in a submicron scale. It presents several **advantages** compared to conventional techniques (i.e. Vickers hardness, tensile tests, etc.) like: (i) the mechanical response can be determined directly without the need to observe the residual imprints, (ii) it can be used in all kind of materials, soft or brittle, and (iii) in every mechanical situation, either elastic or elasto-plastic deformation, the mechanical properties can be obtained [7]. On the other hand, several experimental parameters should be controlled to minimize potential errors, as: (i) corrections needed to be made to taken into account thermal drift, (ii) the equipment has to be thermally stabilized, (iii) vibration of the equipment has to be minimized, and (iv) the indenter shape should be calibrated, making some tests in a standard material with a well-known hardness or elastic modulus (usually fused silica), to calculate the real tip area coefficients and knows exactly the indenter tip geometry.

Nanoindentation technique has a wide range of applications, because it can evaluate the properties of the material in different areas and as a function of the penetration depth. It is especially good for characterization of small volumes, such as coatings or single grains in composites materials, among others [8].

During the indentation process, this technique directly record the applied load (P) vs. the displacement into surface (h) (also known as loading-unloading or P - h curve), while the indenter is displacing into the specimen [9]. The typical data supplied for the nanoindentation tests in the loading and unloading curve is going to be studied on **section 4.3.2**.

Figure 4.1 exhibits a scheme of a nanoindentation device, which consists of three different components: an actuator where the load is applied, a sensor for measuring the indenter displacement and an indenter of specific geometry (blunt or sharp, see **section 4.1**), which is usually assembled to a rigid column through which the force is transmitted.

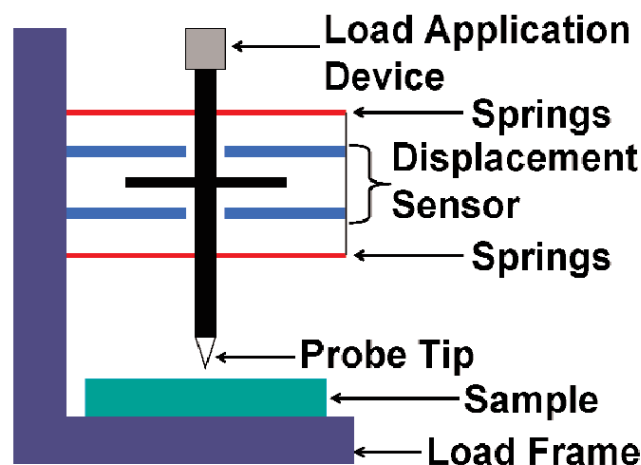


Figure 4.1.- Schematic illustration of an instrumented indentation system [10].

4.1. Tip geometries

Two main different tip geometries can be found: blunt and/or sharp indenters, based in the response produced in the sample during the first stages of the contact between the indenter tip and the specimen of interest (elastic and/or elasto-plastic response, respectively). Normally, both types of tips are made of hard materials in order to avoid the indenter deformation, such as diamond (the usual choice), sapphire, tungsten carbide or boron carbide.

- **Blunt tips**, such as spherical or sphero-conical indenters, are used to study the elastic response of the material, where the unloading curve in the load-displacement diagram is equal to the loading curve and the material does not suffer permanent deformation because of the stress generated under the spherical tip is lower than the yield strength of the material. Using this kind of indenter, the Hertz equations and the Field and Swain method [11,12] the elastic modulus (E) as well as the indentation stress (σ)-strain (ε) curve can be directly predicted. The most common indenter in this category is the spherical tip indenter as it is represented in **Figure 4.2a**.
- On the other hand, **sharp tips** are thought to produce an elasto-plastic deformation since the beginning of the contact. Three side pyramidal indenters are the most used indenter in this group, due to the fact that three sides always converge into a point, while four sides usually create an edge. Among all of three side pyramidal indenters, the most employed indenter in this category is the Berkovich tip (see **Figure 4.2b**) due it has the same projected area than the Vickers indenter. Nowadays, it is still physically impossible to produce a null area, so even the sharp tips have a very low radius as it can slightly appreciate in **Figure 4.2b**. The wear or the use of the tip can

increase its radius, a fact that has to be taken care in very low penetration tests, where elasto-plastic behavior is looked [13].

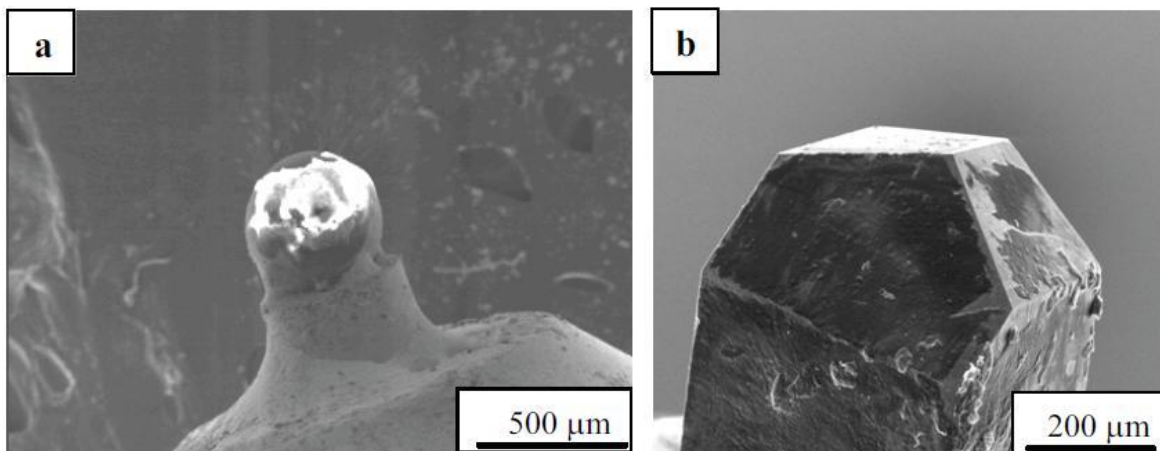


Figure 4.2.- Field emission scanning electron microscopy (FESEM) image of, **a)** Spherical sapphire indenter and **b)** Berkovich diamond indenter [15].

4.2. Continuous stiffness measurements, CSM

Some equipments also have the option of observing the mechanical response as a function of the displacement into surface, using a device coupled to the nanoindenter which allows to perform a continuous stiffness measurements (CSM), which adds a small oscillation, typically of 2nm at 45Hz, superimposed to the load curve as shown in **Figure 4.3** [14]. This allows to record continuously the contact stiffness (S), as well as the mechanical properties (hardness and elastic modulus) as a function of the penetration depth into the specimen. Also this device helps to reduce problems of creep and thermal drift [14].

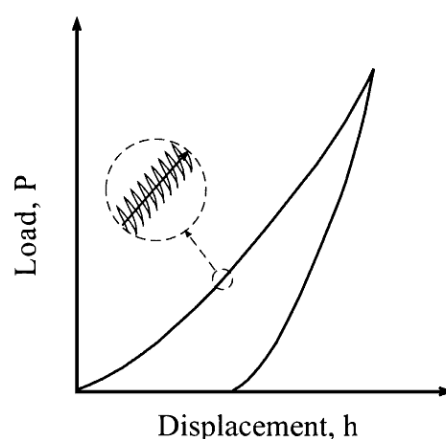


Figure 4.3.- Schematic of the CSM loading cycle [14].

4.3. Contact Mechanisms

4.3.1. Elastic contact

The elastic contact is governed by the Hertz equations [12], which are used to study the elastic deformation field as well as the elasto-plastic transition under spherical contact, see **Figure 4.4**.

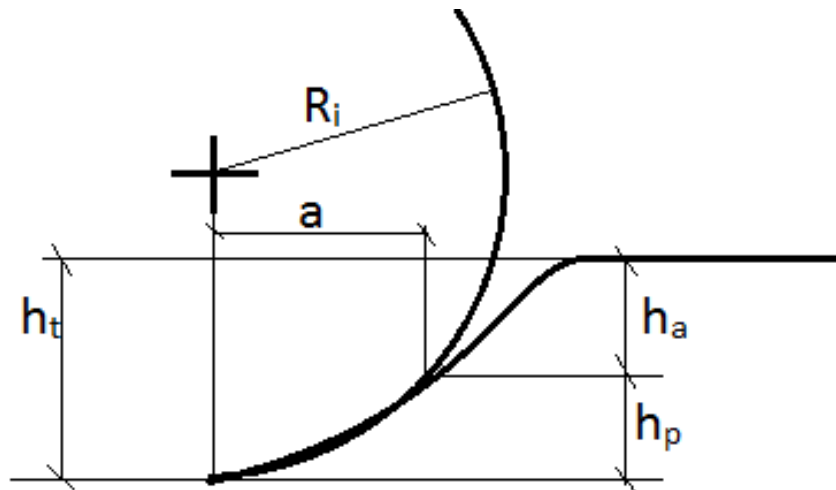


Figure 4.4.- Scheme of a spherical indentation. Where R_i is the indenter radius, h_t is the maximum displacement into surface, a is the contact point, h_a is the deformation induced and h_p is the displacement under the tip.

Hertz defined an equation in which is based all the elastic contact mechanism, and link together the applied load (P), the indenter radius (R) and the elastic properties of the materials in contact, as follows:

$$P = \left(\frac{3}{4} E_{eff} R^2 \right) h_e^{3/2} \quad \text{Equation 4.1}$$

where P is the applied load, R is the indenter radius, h_e is the elastic displacement into surface and E_{eff} the effective elastic modulus of the system tip-studied material, which is given by:

$$\frac{1}{E_{eff}} = \frac{1-\nu^2}{E} + \frac{1-\nu_i^2}{E_i} \quad \text{Equation 4.2}$$

where the subindex (i) is used to represent the indenter material and ν is the Poisson's ratio of each material. If the tip is made of diamond the indenter values are: $E_i = 1141$ GPa and $\nu_i = 0.07$ [7]. Usually, the Poisson's ratio of the studied coating is not known, but using a default value of 0.25 ± 0.1 only produces an uncertainty of about a 5% of the estimated E_{eff} [15] [7].

The contact radius (a) is related to the contact depth of penetration (h_c) through:

$$a = \sqrt{2Rh_c} \quad \text{Equation 4.3}$$

Another important parameter in order to plot the stress-strain curve at micro- and nanometric length scale is the mean contact pressure (p_m). This parameter also known as the Meyer's hardness or indentation stress, which is given by the applied load divided by the contact area, as follows:

$$p_m = \frac{P}{a^2\pi} \quad \text{Equation 4.4}$$

The indentation stress (σ)-strain (ε) curve can be extracted using the following equation:

$$p_m = \frac{4 E_{eff} a}{3 \pi R} \quad \text{Equation 4.5}$$

It is usual to refer p_m as the *indentation stress* and the fraction in the right side of this equation (a/R) as the *indentation strain*. This relationship between p_m and a/R for the coated system shows the existence of a response similar as the obtained with traditional uniaxial tensile tests [16]. Furthermore, the stress-strain curve at micro- and nanometric length scale is also possible to determine for any ceramic material, which is impossible to extract using the traditional uniaxial tensile test machine.

4.3.2. Elasto-plastic contact

When an indentation test is performed, the analysis of the $P-h$ curve obtained by nanoindentation, is based on the work developed by Oliver and Pharr [7], and gives the possibility to acquire some mechanical properties such as the indentation hardness (H) and the indentation elastic modulus (E).

Figure 4.5 shows a typical load on sample (P)-displacement into surface (h) directly obtained using a Berkovich tip indenter.

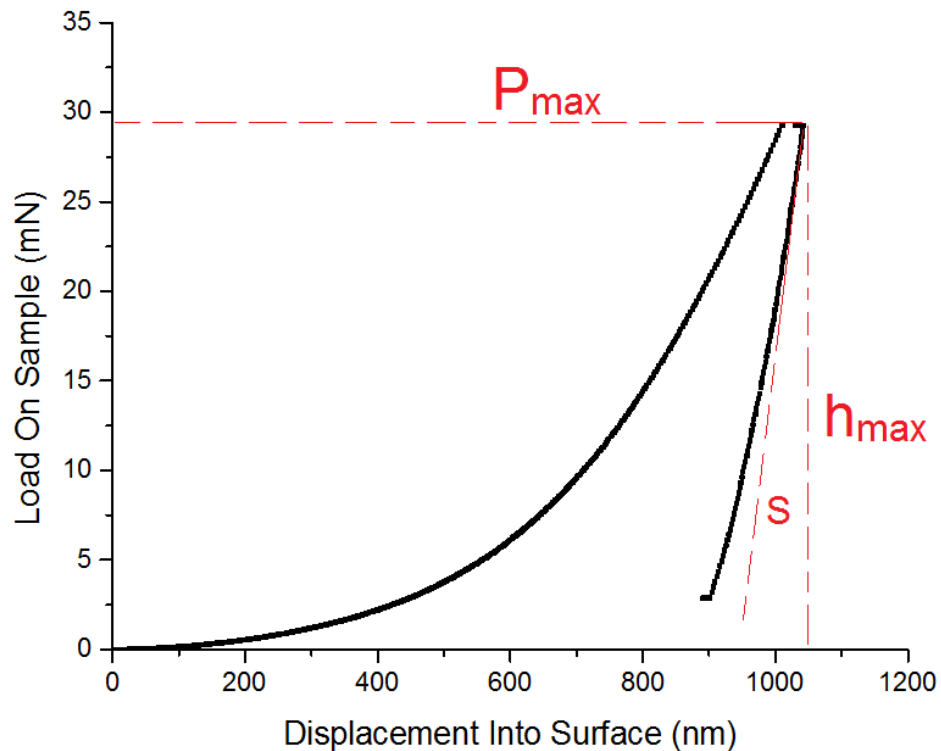


Figure 4.5.- Loading-unloading curve for the 7 85 S sample (see **section 7.1** for description of samples) showing the main parameters. P_{max} is the maximum applied load, h_{max} is the maximum penetration depth, and S is the stiffness measured in the linear part from the unloading curve.

There are some regions that should be commented from this figure:

- The very initial part in the loading curve (<30nm) mainly presents a fully elastic response, so it can be described with the Hertz equation, see **section 4.3.1**, because the indenter tip has some roundness at very small scales.
- When the P - h response gets deviated from the elastic response, it can be said that the local maximum shear stress induced by the indenter is equal to the yield stress of the material, so the sample enters in the plastic regime, and the Oliver and Pharr method [7] can be used to describe this behavior.

As presented in **Figure 4.5** there are several important values of the graph that have to be highlighted: (i) the maximum applied load (P_{max}) or the maximum penetration depth into de sample (h_{max}) depending on which parameter had been used to make the test, the other one can be used as a measure of resistance to the indentation, (ii) the final or residual

penetration depth (h_f) after the indenter tip is removed from the material of interest and (iii) the stiffness (S), which is defined as the slope of the very first stages of the unloading process and has units of load divided per displacement, $S = dP/dh$.

4.4. Mechanical properties determination on coating systems

As described previously, the nanoindentation technique was developed to study the mechanical response of thin films and/or coatings. When the technique is wanted to be used to isolate the mechanical response of a coating of several micrometers thick, the mechanical response will be a function of the h/t ratio for the hardness and a function of h for the elastic modulus, where h is the displacement into the surface and t is the coating thickness. Plotting the mechanical response as a function of the h/t ratio and/or h , shows three different scenarios that can be appreciated: (i) first response (low x -axis values) will be given the mechanical properties of the layer because the elastic and plastic field will be confined inside the coating layer. This situation will led to extract the intrinsic properties of the coating layer without any interaction with the mechanical response of the substrate (see **Figure 4.6a**), (ii) as the indenter moves into the sample (increasing x -axis values without being higher than 1) the elastic and the plastic field will interact with the substrate modifying the mechanical response (see **Figure 4.6b**), and (iii) high x -axis values, the elastic and plastic field will be confined into the substrate. Then, the mechanical response will hold constant to the substrate properties.

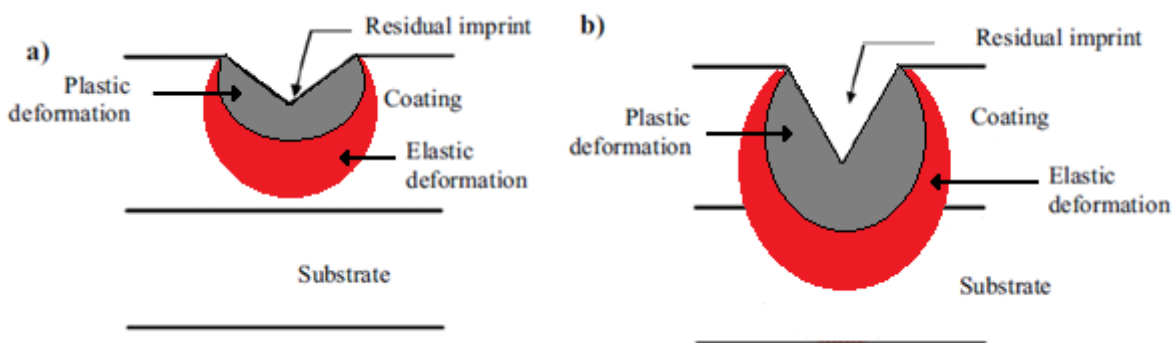


Figure 4.6.- Scheme of a nanoindentation imprint and its deformations where the load or the penetration depth applied is **a)** very low and **b)** high. Adapted from [15].

Hardness and elastic modulus, as a material property, are very difficult to define, due it depends on how it is measured. Indentation tests are widely used, so the hardness and the elastic modulus obtained which it is often called “indentation hardness” and “indentation elastic modulus” to distinguish it from other methods that might be employed [17].

Plotting the **Hardness vs. h/t** for a layered material whose substrate is harder than the coating, the three different regions (see **Figure 4.7**) can be discerned. At low penetration

depths, when the plastic field is confined inside the coating (*1st region*), it is possible to directly determine the coating hardness (H_c). Then, as the indenter goes deeper inside the coating, the plastic field starts to interact with the substrate (*2nd region*) and the hardness starts to increase because it is being affected by the substrate. At higher indentation depth, when the plastic field is confined in the substrate (*3rd region*) the mechanical response keeps constant.

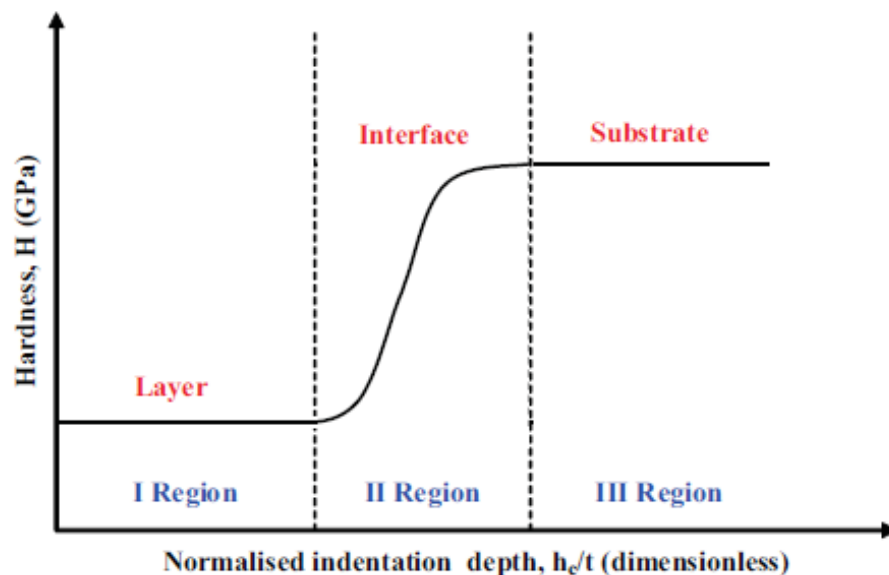


Figure 4.7.- H vs. h/t indentation graph [15].

In order to directly extract the coating hardness (H_c) without interaction with the substrate, several models can be applied, such as: the Oliver and Pharr method [18] or Tuck *et al.* [19], among others. However, one of the widely approximations employed for determining the instrumented hardness of a coating is known as 10% rule. It is mainly accepted that the response of an indentation with a penetration depth of no more than a 10% of the coating thickness is not affected by the substrate. This is known as the “10% rule” and it is used to have an idea of how hard is the material.

Plotting the **effective elastic modulus (E_{eff}) vs. penetration depth (h)** (Figure 4.8) for a coated material, also three different regions can be distinguished. However in this case the *1st region* is smaller, reaching the interface zone with lower penetration depth due to the elastic field is bigger than the plastic one.

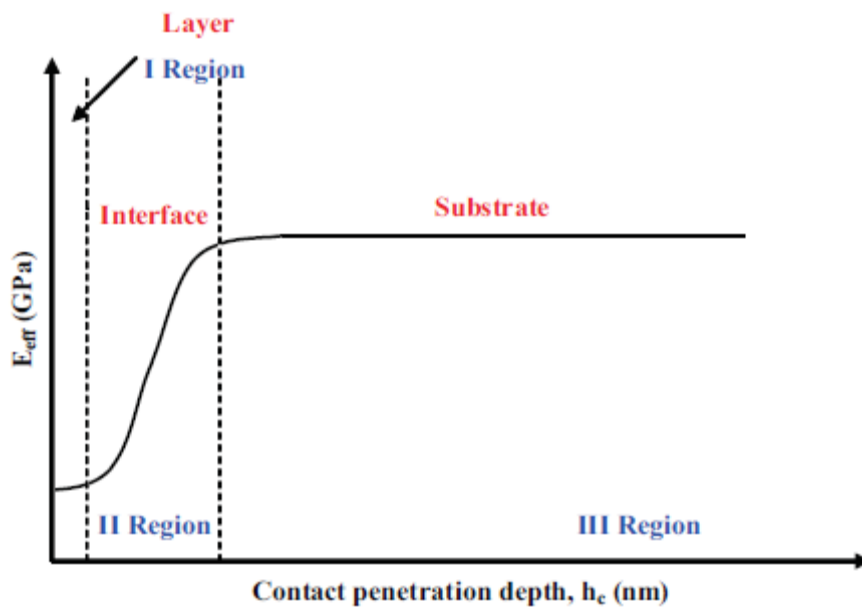


Figure 4.8.- E_{eff} vs h indentation graph [15].

In this case, the measurement of the coating elastic modulus (E_c) presents the same difficulty as the hardness, but, as noticed in **Figure 4.6**, the volume of material affected by elastic deformation during the indentation is bigger than the plastic field. So, in this case a “1% rule” may be applied in order to have an estimation measurement of the coating’s elastic modulus. However, in order to have reliable results at depths around 1% of the thickness the environmental conditions (i.e. temperature, humidity, among others) must be well controlled and the tip has to be carefully calibrated for penetration depths lower than 10 nm for a coating of 1 μm . Furthermore, if the results at that depth have too much scatter it is also possible to extrapolate the elastic modulus against penetration depth graph, from the plateau of the first region until the beginning of the graph ($h = 0$ nm), founding the elastic modulus of the coating without any contribution of the substrate. However, this process is only an approach and for some coatings does not work properly. In the literature exists several analytical or parametrical models and/or approaches in order to isolate the elastic modulus for the coating, which are based in adjusting the $E_{\text{eff}}-h$ curves, as Bec et al. [20], Saha and Nix [21], Rar et al. [22] or Jagger [23], among others, which try to parameterize the $E_{\text{eff}}-h$ curve, as seen in **Figure 4.9**.

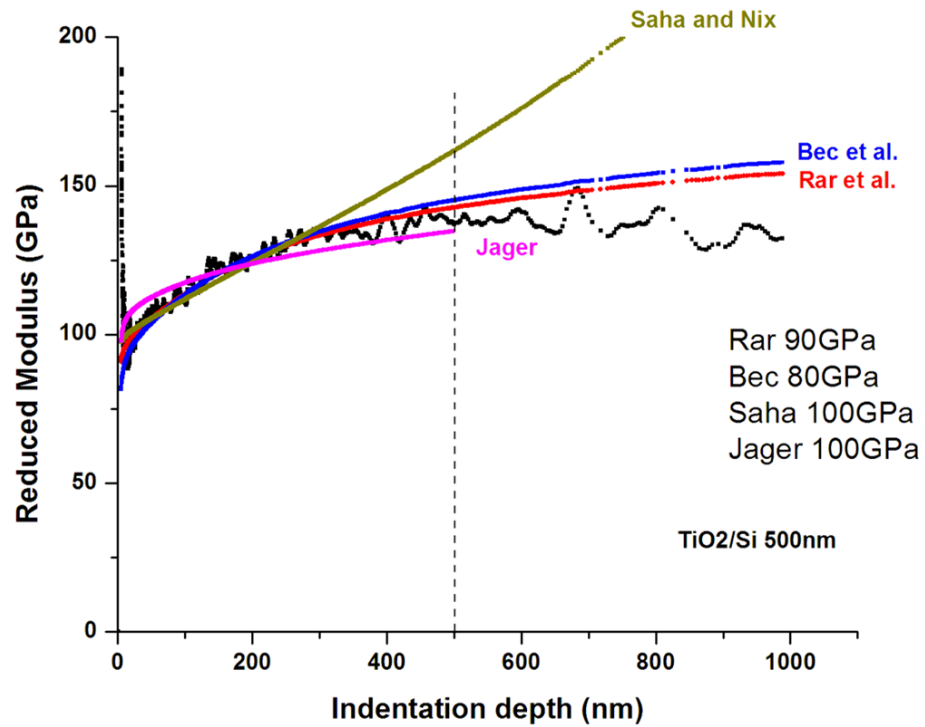


Figure 4.9.- E_{eff} vs h graph for TiO₂/Si system adjusted with several models [13].

4.5. Tribological characterization of coatings

To characterize and better understand the adherence between the coating and the substrate as well as to induce different damage along the sliding track, some tribological experiments using the nanoscratch technique can be used. This technique is similar to the indentation but, while the load is applied, the sample is moved, in order to induce severe damage to the sample, see **Figure 4.10**. During the nanoscratch test, the friction coefficient evolution between the indenter tip and the specimen (not shown in this project) is recorded at the same time.

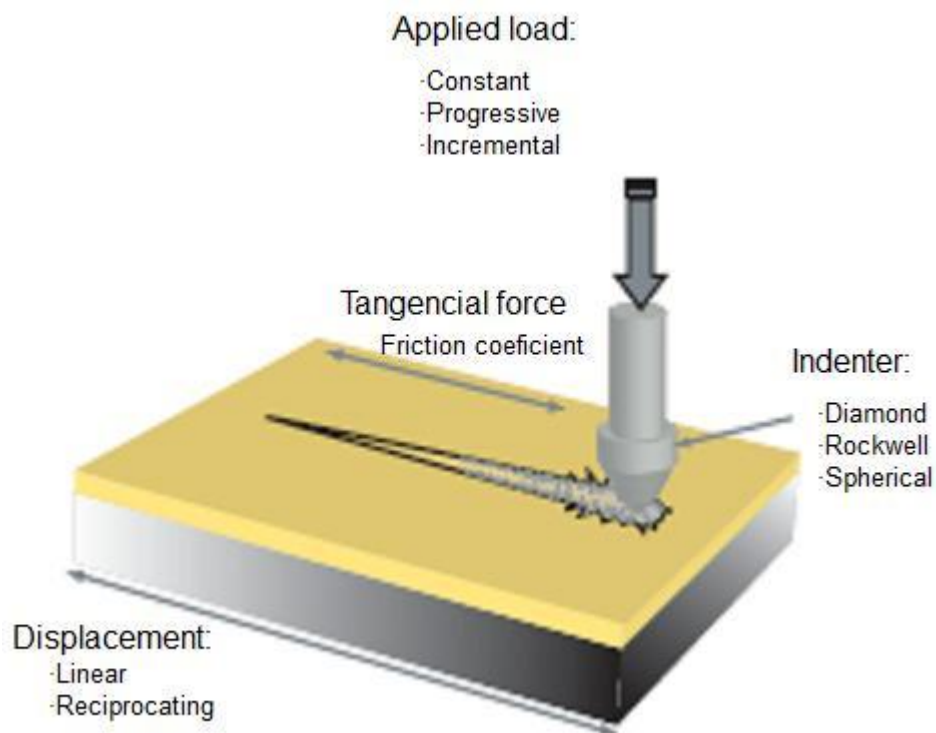


Figure 4.10.- Schematic representation of a scratch test [24].

As shown in **Figure 4.10**, there are different types of scratch, as if the load is constant or if it is incremental (changes along the track distance), or how the displacement is made.

The tribological characterization made was based in the critical load parameter (P_{cr}), which can be evaluated using another parameter named critical length (L_{cr}). The tribological procedure is described below:

- i) Using microscopy, the scratch path and the initial damage can be observed.
- ii) Measure the length between the starting point of the scratch to the first damage. That distance will be L_{cr} .
- iii) Knowing that the load applied increases linearly, it is possible to extract the P_{cr} where superficial damages (i.e. Chevron or radial cracks, etc.) are appreciated by optical techniques.

5. State of the Art

Scarce information about the mechanical properties at micro- and nanometric length scale using sharp indentation of the microcolumnar structure studied in this thesis are available in the literature. Gaillard *et al.* [3] studied TiO₂ tilted coatings over a Si substrate with a glancing angle technique to prepare the samples with different growing angles: 60°, 80° and 90°. Recently, Jiménez-Piqué and co-workers [4] studied the same set of specimens with different coating structure, either tilted or zig-zaged.

Table 5.1.- Summary of the main parameters reported in the literature for similar set of specimens studied in this project.

Author	Coating	Substrate	Growing structure	Hardness, <i>H</i> (GPa)	Elastic Modulus, <i>E</i> (GPa)
Gaillard <i>et al.</i> [3]	TiO ₂ 60°	Silicon	Tilted	1.61	51 ± 9
	TiO ₂ 80°			0.15	21.5 ± 13
Jiménez-Piqué and co-workers [4]	TiO ₂ 90°	Silicon wafer	Tilted	0.1	20 ± 15
	TiO ₂ 60°		Zig-zaged	1.60 ± 0.10	43 ± 2
			Tilted	1.68 ± 0.08	41 ± 1
	TiO ₂ 70°		Tilted	0.84 ± 0.07	26 ± 3
			Zig-zaged	0.95 ± 0.05	24 ± 2
	TiO ₂ 80°		Tilted	0.30 ± 0.06	12 ± 4
	Zig-zaged	0.31 ± 0.07	10 ± 2		

6. Objectives

The main activities of this project were focused to try to correlate and understand the mechanical behavior as a function of the coating microstructure as well as to observe how these coatings behave under sliding conditions. Then, the objectives can be summarized in three main goals:

- i) Mechanical properties under uniaxial compression tests:
 - Determination of the mechanical properties (indentation hardness and indentation elastic modulus) for different sets of $\text{TiO}_2\text{-SiO}_2$ coatings showing different microstructures (compacted, tilted, spiral and zig-zaged structure) using sharp indentation.
 - Study the indentation stress-strain curve as well as the elasto-plastic transition and determine the elastic modulus, the mean contact pressure for each set of specimens of interest using spherical indentation.
- ii) Cohesive and adhesive damage in the interface under sliding contact by means of nanoscratch tests.
- iii) Superficial and sub-superficial fracture events induced under different contact modes and tip geometries by advanced characterization techniques (i.e.: confocal laser scanning microscopy, field emission scanning microscopy and atomic force microscopy for the superficial events and focused ion beam for the sub-superficial fracture events).

7. Experimental procedure

7.1. Samples Preparation

The samples of study have been manufactured and provided by the “*Instituto de Ciencia de los Materiales de Sevilla*” [25]. They were, approximately, of 4 x 4 cm² of surface.

The substrate material of the coatings of interest is common glass. Analyzed separately, it was found that its indentation hardness and indentation elastic modulus are around 6 and 70 GPa, respectively. The glass was coated with three different numbers of layers, with a constant bilayer period (λ) of TiO₂-SiO₂ of 170 nm.

The different sets of coated samples to be studied could be separated in three different groups as it is summarized in **Table 7.1** and schematized in **Figure 7.1**.

Table 7.1.- Differential parameters of the coatings.

Number of layers	Growth orientation	Growth pattern
-	-	Compact
3	70	Spiral
7	85	Zig-zaged
15	-	Tilted

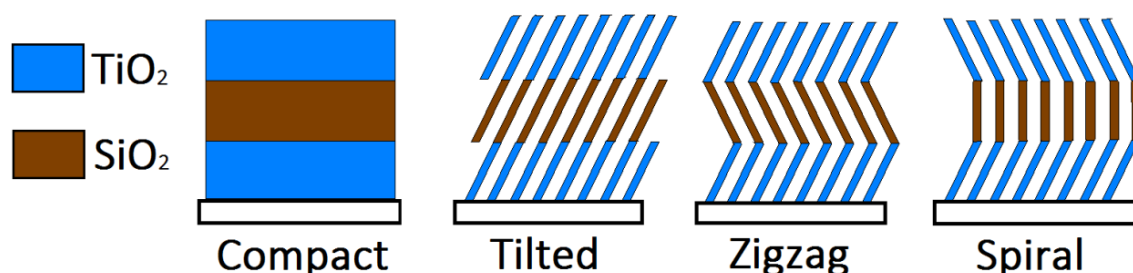


Figure 7.1.- Schematic representation for the three layered coatings investigated in this project. The TiO₂ and SiO₂ layers are represented in blue and brown, respectively.

All the coatings were made using the GLAD technique (for more information see **section 3.2.2**), in a chamber with oxygen pressure of approximately 0.01 Pa to ensure the complete

oxidation of the evaporated oxides. The thickness of each individual layer was controlled by means of a quartz crystal monitor calibrated with the actual thickness of layers determined by cross section and observed by scanning electron microscopy, SEM [25].

After that, all the samples were marked to identify the correct orientation of the coating columns. The mark had been done in the coating free face, and it is placed in the right corner of each specimen. When the mark is seen up-right and lower-left (see **Figure 7.2a** and **7.2b**, respectively), the surface that is being seen is the one that have the coating, with the first layer of columns pointing up. In **Figure 7.2c**, is shown in perspective the first column orientation.

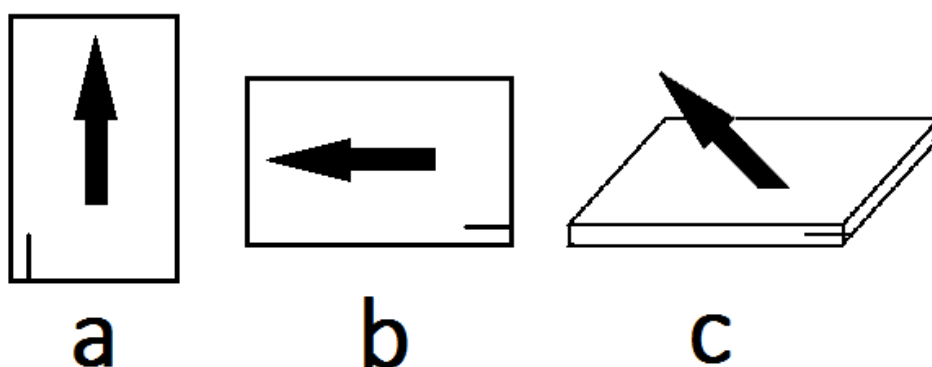


Figure 7.2.- Sketch of the samples received were it can be seen the mark that shows the column orientation. **a)** and **b)** frontal view and **c)** lateral view where the first column orientation is showed.

The samples were first studied under a magnifying glass, changing the light direction, in order to determine if the coating was in the right surface and to see its conditions. As can be seen in **Figure 7.3**, there were lots of differences between a sample and another, due the increasing number of layers that make the light to be more reflected.



Figure 7.3.- Optical differences between the samples. From left to right: 3 70 S, 7 70 S and 15 70 S.

Because of the high number of samples received, and the similarity between them, a certain code was needed to help identifying one from another.

The code employed in this project consists of three different parts: the first one was a number used to indicate the number of layers of the sample, the second part was also a number, which indicate the growing angle, and the third was a capital letter explaining the shape of the different coating. The code employed in this project is summarized in **Table 7.2**.

Table 7.2.- Code used in this project.

Number of layers	Growth orientation	Growth pattern
-	-	C
3	70	S
7	85	Z
15	-	T

Where **C**: compact, **S**: spiral, **Z**: zig-zag and **T**: tilted.

So, if one sample is named 7 85 S, the sample which is being referred is the one that has 7 layers which are 85° tilted from the normal surface, and the nanocolumns present a spiral pattern. But not all the possible combinations between the three columns could be made, as the compact growth pattern does not present any growing orientation due the compact layer is completely flat and cannot be deposited with any angle.

Once the samples had been observed and the coated face determined, it was thought that, in order to have an “*extra sample*” of everyone, the samples were cut in some small parts

(0.5 x 0.5 cm²), one of them used to do the mechanical tests and the other pieces to be stored.

The different specimens were cut using a diamond tip pen. After that, were glued into an aluminum stub with silver colloidal glue and the extra specimens were stored in a plastic box.

7.2. Mechanical characterization

The mechanical characterization of the coating layer was done by Nanoindentation technique using a Nanoindenter XP (MTS), see **Figure 7.4**.

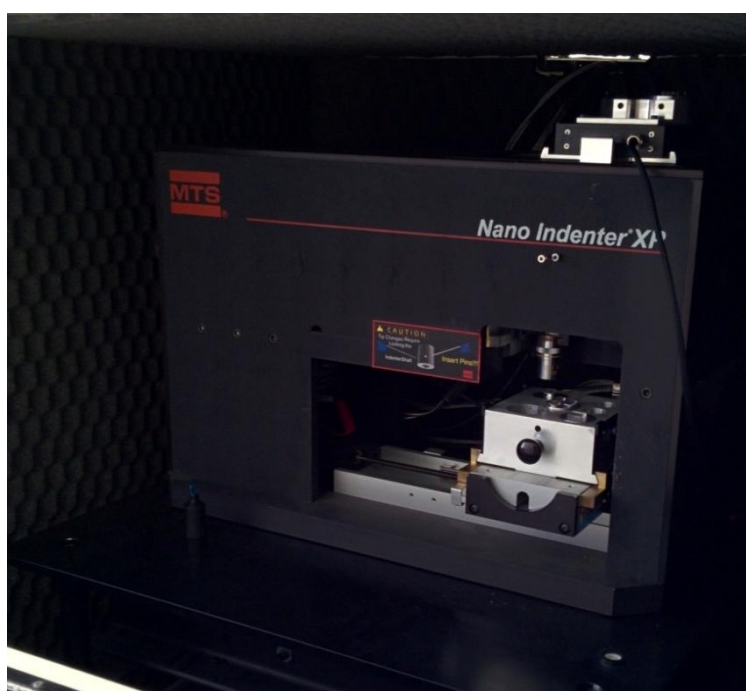


Figure 7.4.- General view of the nanoindenter employed along the project.

Three different sets of experiments were done at micro- and nanometric length scale using the Nanoindentation technique:

i) Hardness and elastic modulus determination by means of sharp indentation:

The first tests were made to all the samples using a calibrated Berkovich diamond tip, and experimental data were analyzed using the Oliver and Pharr method [7,18]. Three different sets of homogeneous arrays (4 by 4 imprints) were done at different penetration depths: 1000, 500 and 200 nm as it can be depicted in **Figure 7.5**. The separation between two indentations was calculated and kept constant to 50 μm , 20 μm and 10 μm for the 1000, 500 and 200 nm of indentation depth,

respectively, in order to avoid any overlapping effect. After that, using the 10% rule and the extrapolation to zero, the hardness and elastic modulus were determined, respectively.

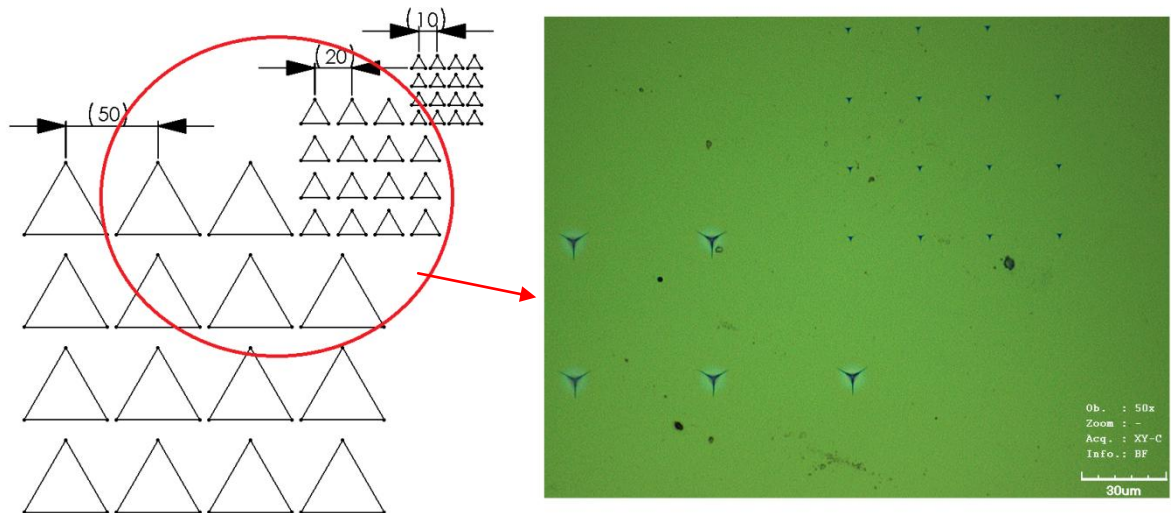


Figure 7.5.- Schematic of the situation of the three indentation matrices (left hand side) and a LSCM image of the marked zone (right hand side).

- ii) **Indentation stress-strain curve:** For the 7 70 specimens, an homogeneous array of 9 imprints (3 by 3) at 10 mN of maximum applied load and separated 250 μm one from the other in order to avoid any overlapping effect were made using a 50 μm diameter diamond tip. The experimental data were analyzed using the Hertz equation [12].
- iii) **Nanoscratch tests:** Two different sets of tribological tests were done: The first one was made along of a random direction, with the load applied increasing lineally (from 0 up to 50 mN) along the scratch track reaching a maximum length of 200 μm as it can be appreciate in **Figure 7.6**.

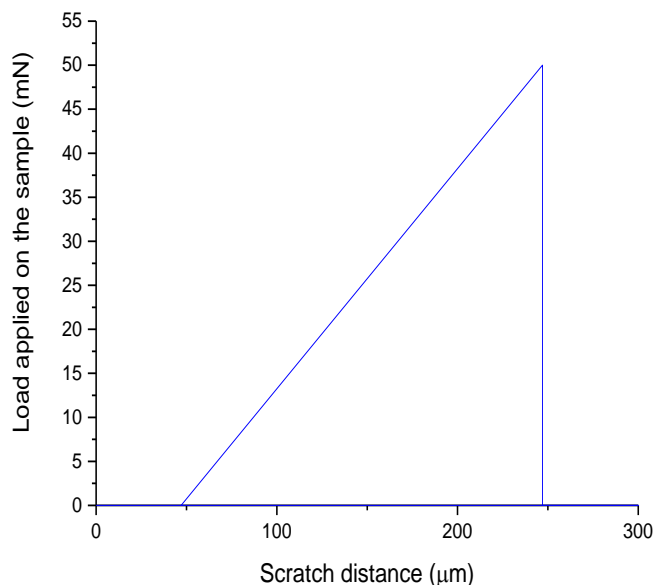


Figure 7.6.- Graph representing the evolution of the applied load along the scratch track.

The second type of test was made in four directions along the sample for the 7 70 specimens, in order to comb the coating columns in every direction and see if these coatings present any anisotropy effect in terms of the critical load, P_c as well as the damage activated for each direction. The test was only performed in 7 70 samples in order to study the relationship between the mechanical properties and the growing structure. A scheme of the different sets of scratches done in the 7 70 specimens can be observed in **Figure 7.7**. The applied load was increased from 0 mN until 30 mN in a track of 500 μm.

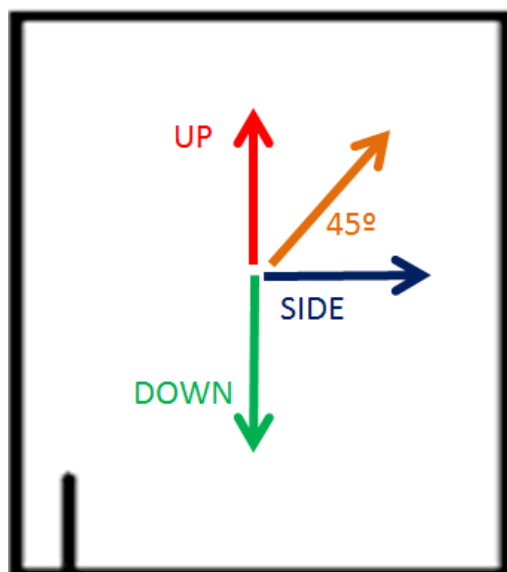


Figure 7.7.- Schematic of the four directions scratched for the 7 70 specimens.

7.3. Superficial observation

Surface observations of the residual imprints performed at different penetration depths as well as the nanoscratch track were performed using advance characterization techniques: laser scanning confocal microscopy (LSCM), field emission scanning electron microscopy (FESEM) and atomic force microscopy (AFM).

7.3.1. Laser Scanning Confocal Microscopy, LSCM

A light microscope has a resolution of 0.2 μm and it only allows creating flat images, whereas a confocal laser microscope can go up to 0.12 μm in xy -plane and 0.01 μm on z -direction, which allows the user to perform 3D reconstructions [26].

Figure 7.8 shows a schematic of the LSCM used:

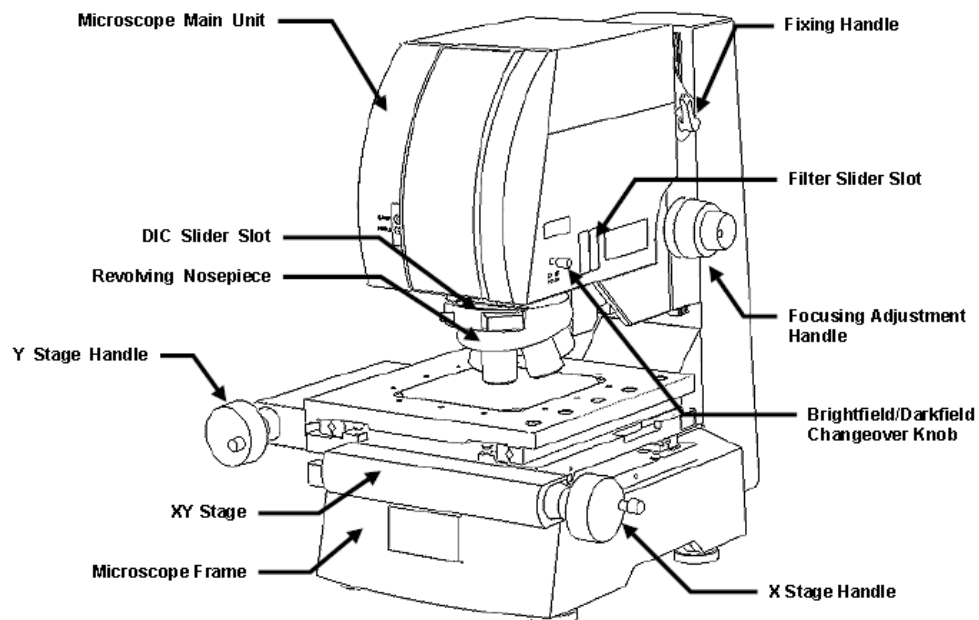


Figure 7.8.- Schematic of OLS3100 Confocal Laser Microscope [26].

All the imprints as well as scratch track, were observed by laser scanning confocal microscopy, LEXT OLS using 5x, 10x, 20x, 50x and 100x optical zoom and from 1x to 6x of an electrical zoom that can be used to amplify the image, losing some resolution. The equipment also had an isolation stage in order to avoid any vibration to distort the image during the acquisition process.

7.3.2. Field Emission Scanning Electron Microscopy, FESEM

A scanning electron microscopy (SEM) uses a high energy electron focused beam thrown into the sample. The electrons are usually generated by heating a tungsten filament, and they are used to interact with the surface of the sample producing different signals that are analyzed and treated to reveal microstructural information of the sample such as the external morphology, the crystalline and orientation structure or the chemical composition [27].

The field emission scanning electron microscopy (FESEM) is a SEM based technology, where the terms “*field emission*” are related to the emission of electrons from the conductor’s surface caused by a strong electric field, whose acceleration voltage between cathode and anode is in 0.5-30 kV range. The microscope requires a high vacuum (rounding the 10^{-6} Pa) to operate, and its resolution is on the order of 2 nm at 1 keV or 1 nm at 15 keV [28]. A scheme of FESEM equipment can be appreciated in **Figure 7.9**.

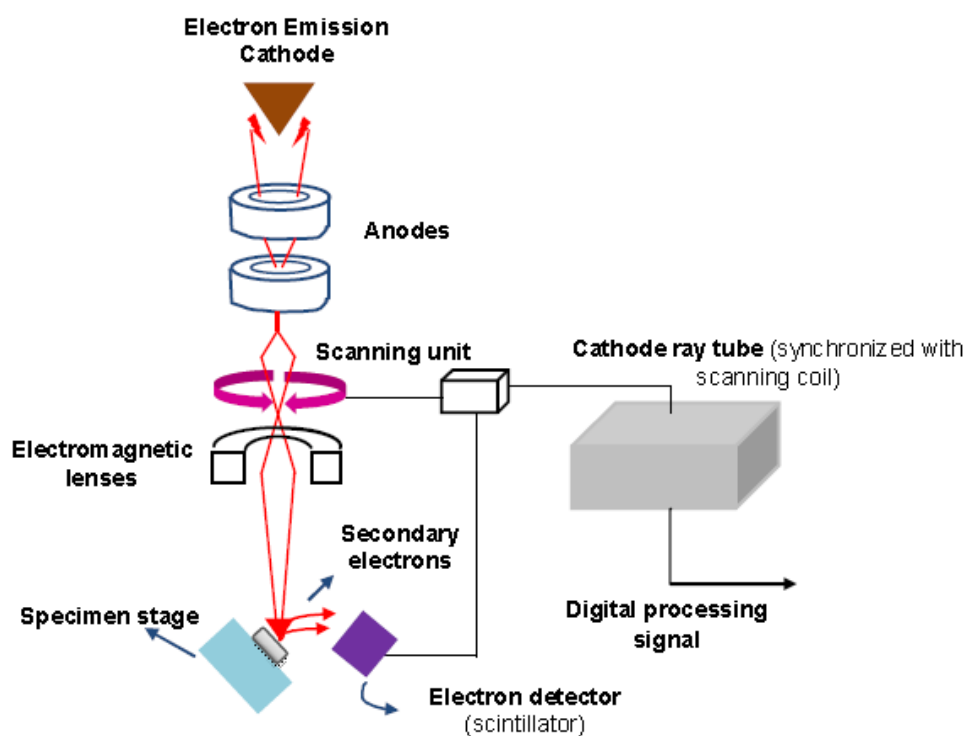


Figure 7.9.- FESEM representation [28].

One of the notorious disadvantages of using a FESEM, is that the sample has to either be conductive or been sputtered with a conductive coating, mainly carbon. The coatings of study were not conductive, so they had to be sputtered with carbon layer of several tens of nanometers.

The superficial damage around the residual imprints as well as the nanoscratch tracks were observed by using the field emission scanning electron at 20 kV.

7.3.3. Atomic Force Microscopy, AFM

An atomic force microscopy (AFM) is a microscopy based in the measurement of forces between a sharp probe and the studied surface, in which separation between them normally is under 10 nm, and it is able to generate a 3D profile of the sample's surface with a scale from millimeters to nanometers [29].

The probe is linked with a flexible cantilever, which oscillates, moving the probe against the sample. This oscillation is used, using a laser beam, to calculate the z-position in which the probe finds the sample.

A schematic of the working process is shown in **Figure 7.10.- Schematic of the AFM.**

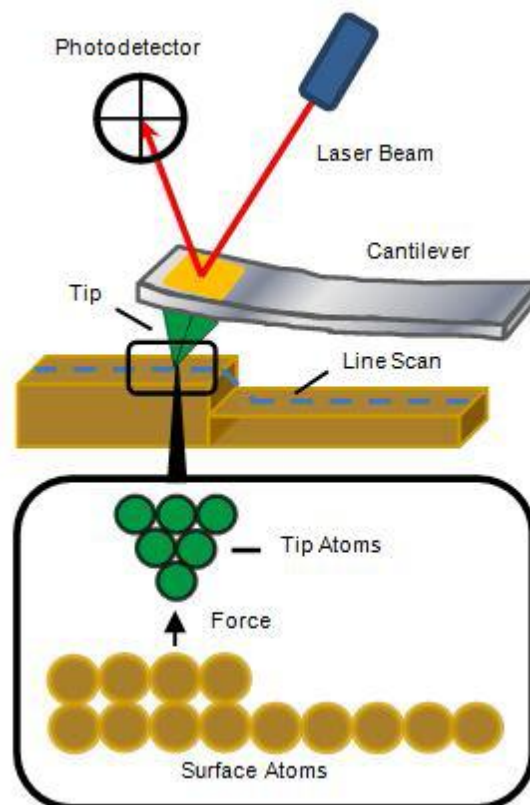


Figure 7.10.- Schematic of the AFM technique [29].

The AFM can operate in three different modes [29]:

- a) **Contact mode:** the probe-surface separation is less than 0.5 nm. The cantilever bends if its spring constant is less than the surfaces. By maintaining a constant cantilever deflection, the force applied is constant, and an image of the surface can be obtained.

- b) Tapping mode:** this mode uses a probe-surface separation between 0.5 and 2 nm, the cantilever oscillates at its resonant frequency (~ 50-500 Hz depending the type of cantilever) and the probe only taps the surface at the lowest point of the wave. By maintain constant the oscillation frequency, the tip-surface interaction is maintained and an image of the surface can be obtained.
- c) Non-contact mode:** this mode has the larger probe-surface separation (around 0.1 – 10 nm) and is used to measure the attractive Van der Waals forces between the probe and the liquid absorbed by the surface.

All the images obtained during this study have been recorded working on tapping mode, where the laser beam was focused in the middle of the photodetector, which has a -1 V to 1 V displacement. Furthermore, this technique allows to recorder three different AFM images at the same time, which can be used for different proposals:

- **Phase image:** that can be used to estimate the phase composition of the sample, which is not easy to evaluate (this kind of image will not be used along this project).
- **Error image:** is made by the photodetector displacement, its scale is in voltage units.
- **Topographic image:** is the integrated image of the error image, its scale is in units of length, and can be observed as a real representation of the sample. This AFM image is the most useful image obtained during the scan.

The residual imprints made by Berkovich tip indenter were observed by an atomic force microscopy (AFM, Dimension D3100) from Bruker working on tapping mode. All the AFM images were processed with the WSxM software [30].

7.4. Sub-Superficial observation

The sub-superficial observation was done by means of Focused Ion Beam (FIB), which works similar as a FESEM, both of them use a focused beam to scan the samples. FIB technique uses an ion beam, whereas the FESEM uses an electron beam.

As shown in **Figure 7.11**, the ion beam is generated from a liquid metal (Ga^+ alloy) and focused towards the sample using electrostatic lenses. Operating with low beam currents allows to image the sample, when high currents are used sputtering or milling processes can be performed [31].

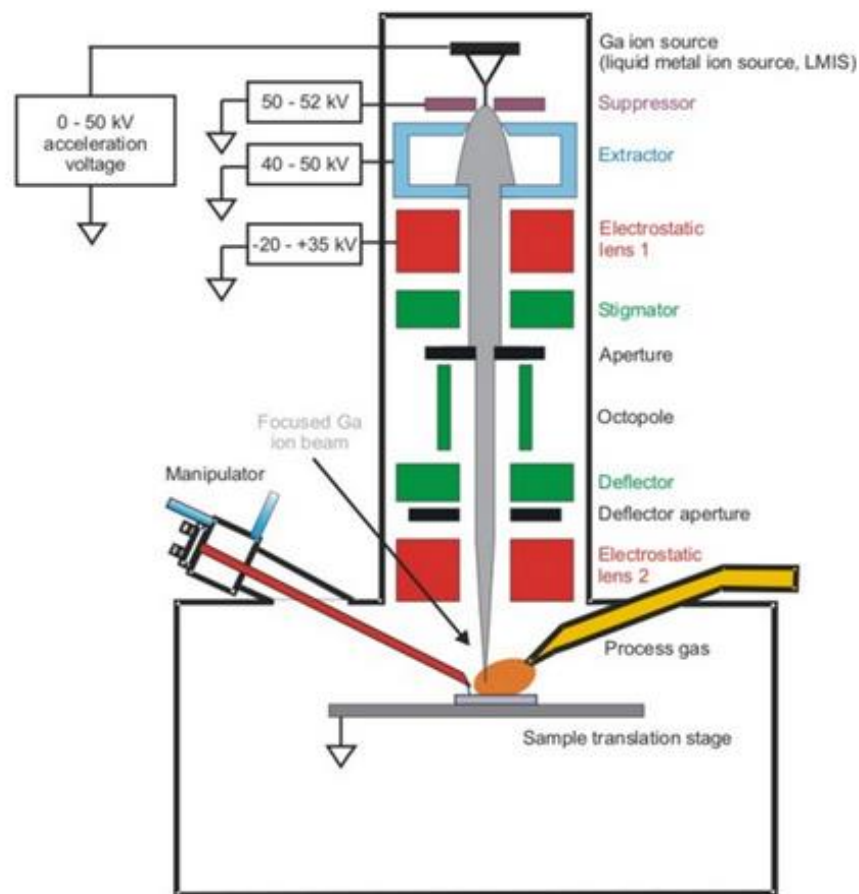


Figure 7.11.- Schematic representation of a FIB system [31].

One of the most used applications of FIB is to be used jointly with FESEM, where FIB mills the sample and FESEM images. So a sub-superficial observation of the sample can be done, see scheme represented in **Figure 7.12**.

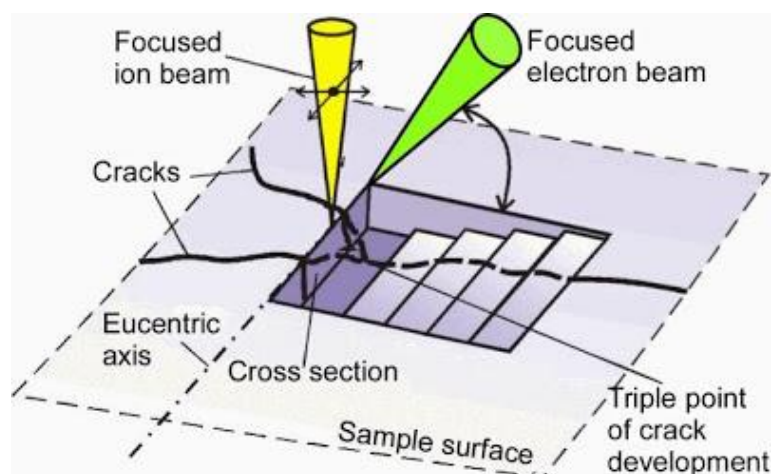


Figure 7.12.- Schematic representation of a FIB/FESEM system [32].

Cross sections of regions of interest were done by focused ion beam/field emission scanning electron microscopy (FIB/FESEM) using a Zeiss Neon 40 system from Carl Zeiss. A platinum layer of around 1 μm was initially deposited prior milling in order to prevent the superficial integrity of the specimen before the milling process. A Ga^+ ion source was used to mill the surface at a voltage of 5 kV. The final polishing of the cross-section was performed at a current of 500 pA and 5 kV acceleration voltage.

8. Results and Discussion

8.1. Mechanical Characterization

8.1.1. Hardness

As explained in **section 7.2**, the different indentation tests performed were treated using the Oliver and Pharr method [7], as it is shown in the following figures. As it can be appreciated, the substrate is harder than the coating, that's why when the indentation tip reaches the 10% of the coating thickness, the hardness recorded by the nanoindenter is plateau and starts to increase, reaching a hardness value slightly lower than the substrate (glass) hardness.

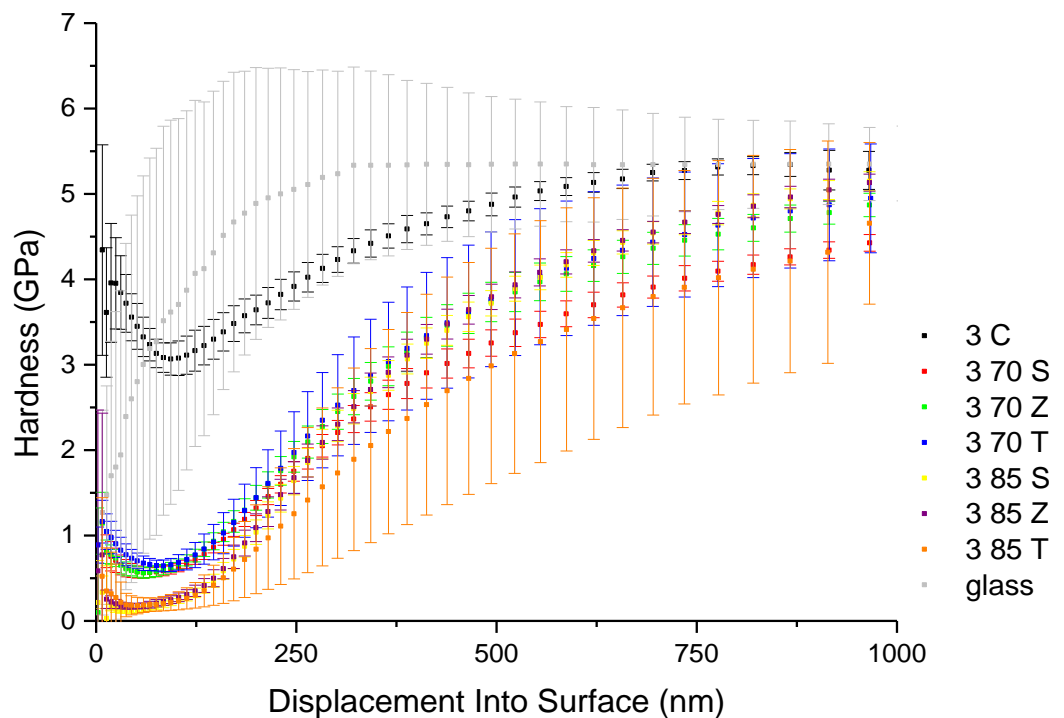


Figure 8.1.- Hardness evolution for the coating/substrate of study against the displacement of the indenter for the different specimens of interest with three deposited layers. The hardness evolution for the substrate (gray curve) has also been investigated for comparison purposes.

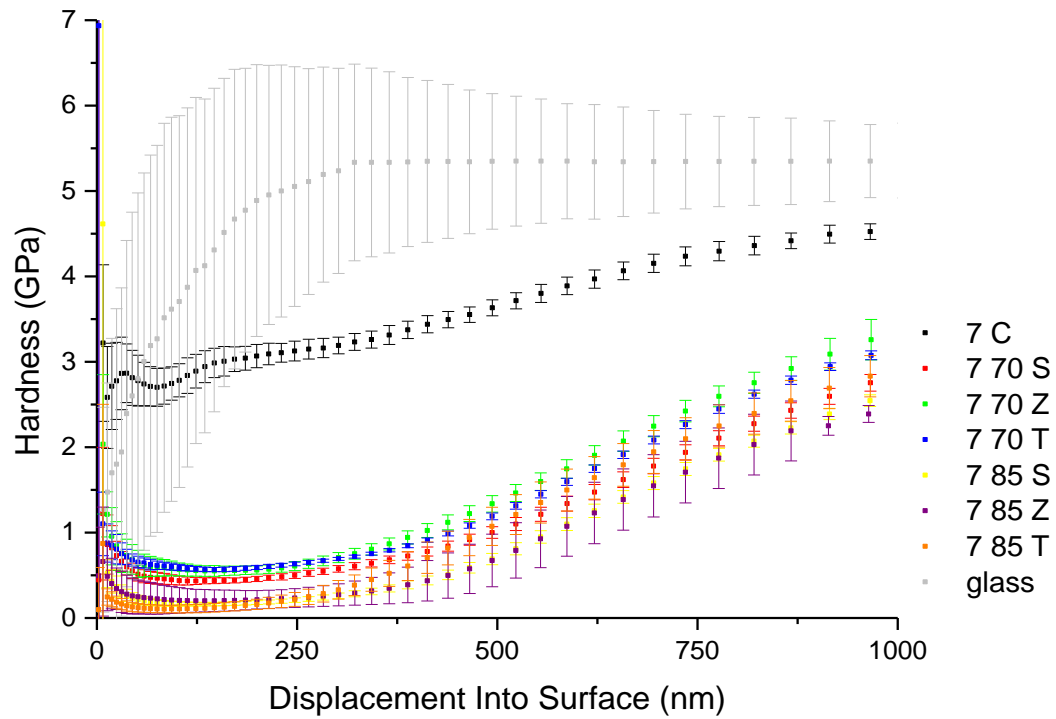


Figure 8.2.- Hardness evolution for the coating/substrate of study against the displacement of the indenter for the different specimens of interest with five deposited layers. The hardness evolution for the substrate (gray curve) has also been investigated for comparison purposes.

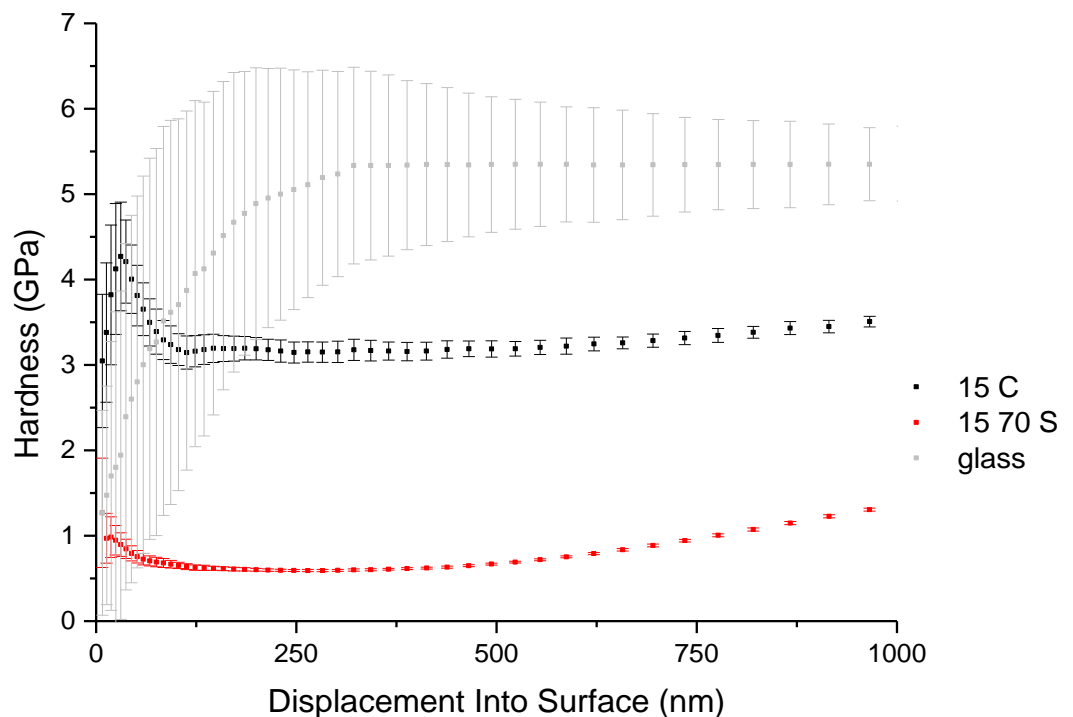


Figure 8.3.- Hardness evolution for the coating/substrate of study against the displacement of the indenter for the different specimens of interest with fifteen deposited layers. The hardness evolution for the substrate (gray curve) has also been investigated for comparison purposes.

As it can be appreciated in **Figure 8.1**, **Figure 8.2** and **Figure 8.3**, for low values of displacement into the surface, the hardness evolution presents a constant plateau, being possible to directly determine the intrinsic coating hardness using the 10% rule without the influence of the substrate. Thus means, that the plastic field induced by the Berkovich tip indenter at that displacement into surface (around 10% the coating thickness) is confined inside the coating. **Figure 8.4**, **Figure 8.5** and **Figure 8.6** show the hardness evolution through the normalized displacement into surface, h/t (displacement into surface divided by the coating thickness).

It has to be noticed that a test performed at the same penetration depth will not reach the same ratio displacement/thickness in a few layers coating or in a several layers coating. Due that, the test performed at 1000 nm of penetration depth had two different responses. While in the 3 layers and the 7 layers samples the indenter tip reached and penetrated into the substrate, in the 15 layers samples, the indenter tip nearly reached the three quarters parts of the coating. This behavior can be associated with the different damage events activated during the indentation process. This behavior will be discussed in detail in **section 8.2**.

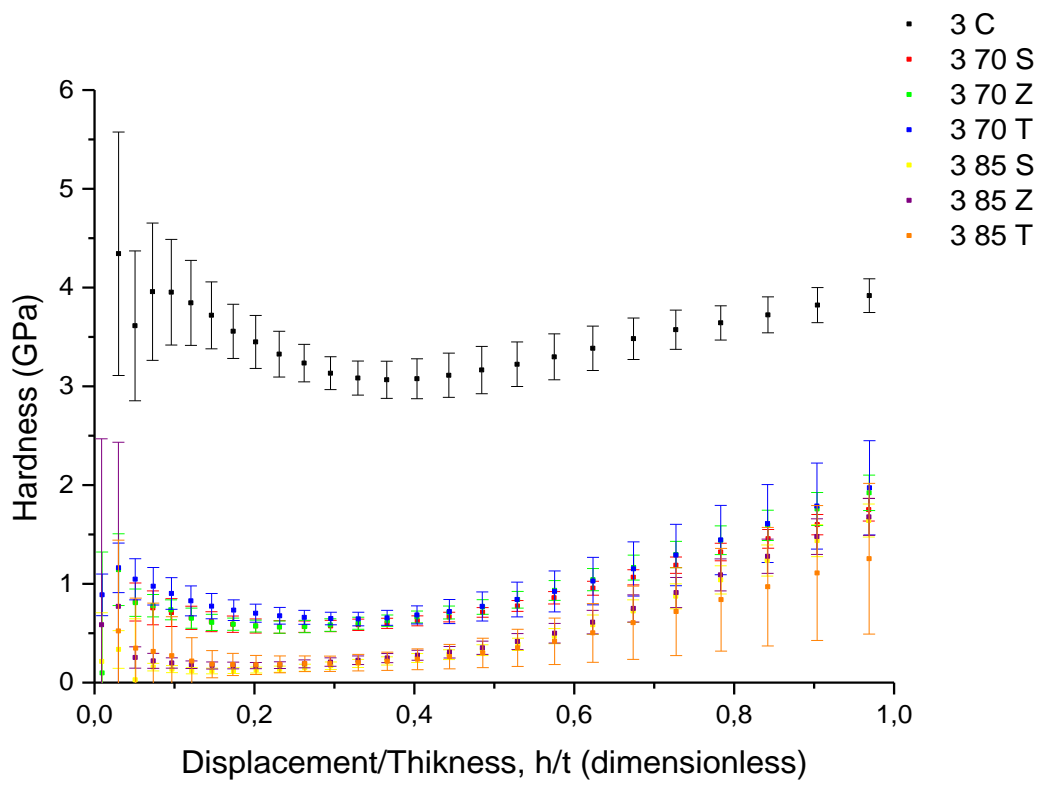


Figure 8.4.- H vs h/t evolution for the three layered samples of study.

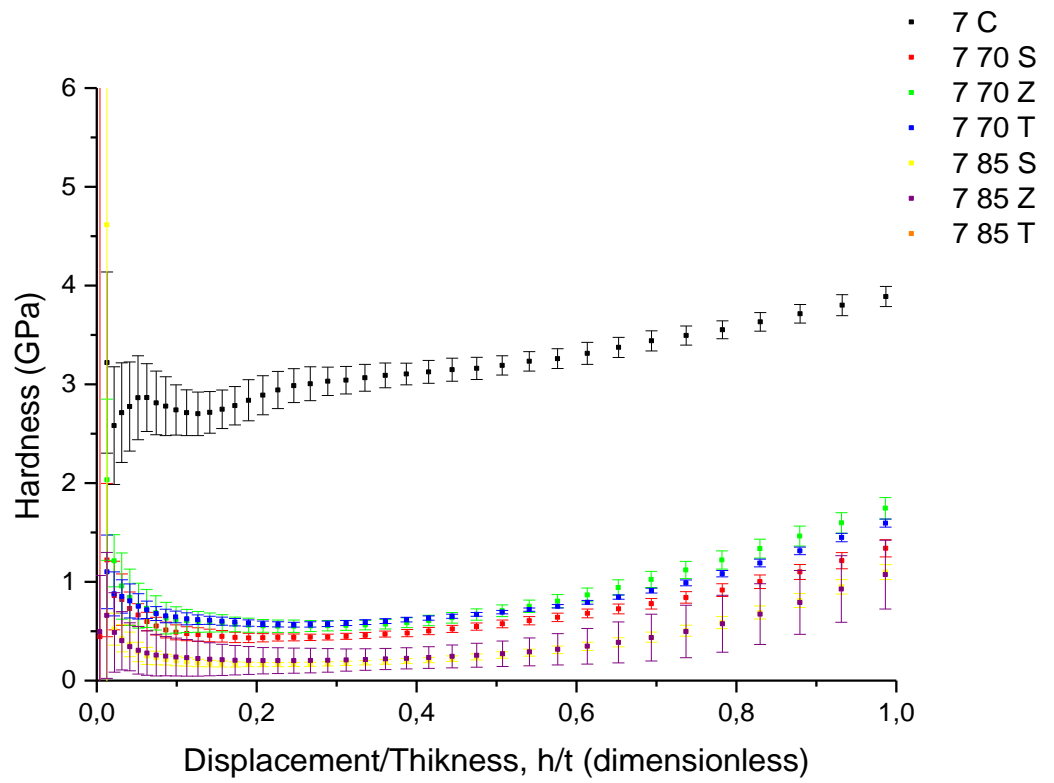


Figure 8.5.- H vs h/t evolution for the five layered samples of study.

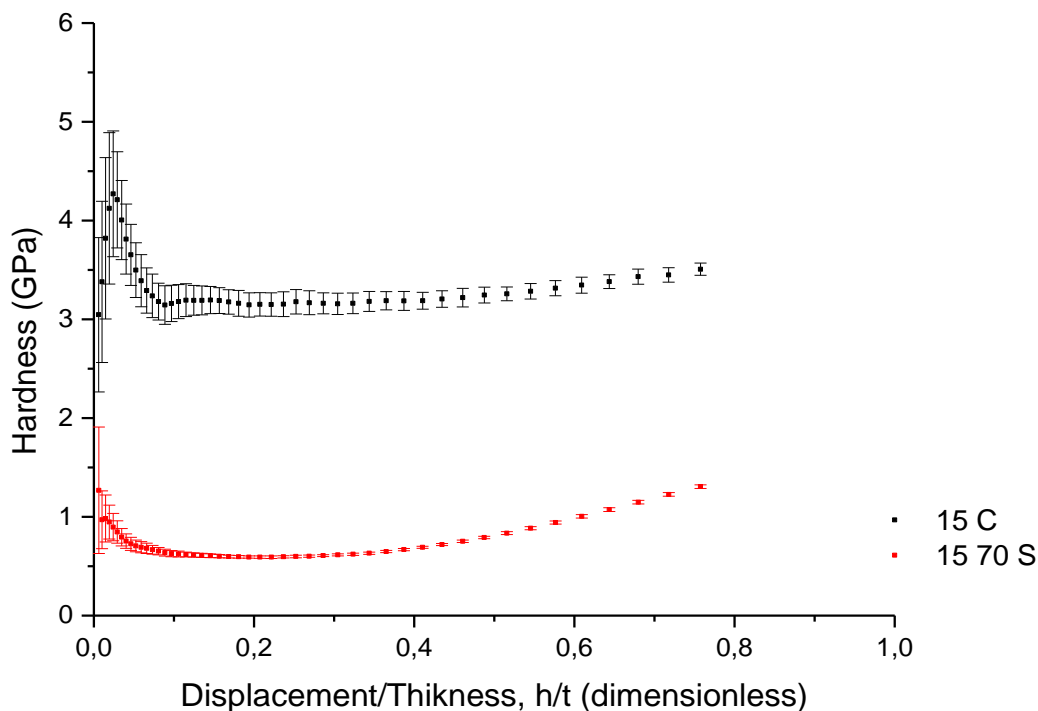


Figure 8.6.- *H vs h/t evolution for the three layered samples of study.*

Table 8.1 sums up the thickness and the penetration depth needed to extract the hardness of each sample without the influence of the substrate.

Table 8.1.- Coating thickness and penetration depth needed to extract the H_c .

Number of layers	t (nm)	t _{10%} (nm)
3	255	25.5
7	595	59.5
15	1275	127.5

Figure 8.7 shows the summary of the coating hardness for each specimen, trying to identify if exist any trend between the coating microstructure and the local mechanical properties in terms of hardness. As three different sets of tests were made using different penetration depths, there are three values for each sample, which can be helpful to validate the results.

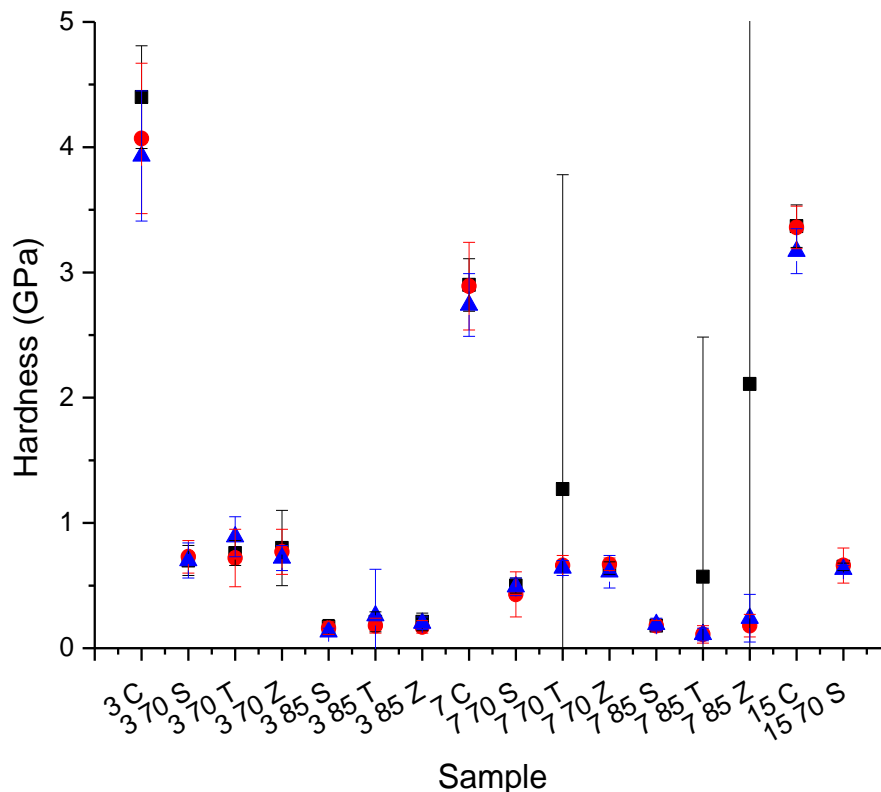


Figure 8.7.- Hardness extracted for each sample using the 10% rule. Black, red and blue marks correspond with the data obtained through imprints performed at 200, 500 and 1000 nm of maximum displacement into surface, respectively.

As can be seen, the mechanical tests done at the lowest displacement into surface (~ 200 nm, black marks), were the ones which provide much more deviation. This phenomena can be related with the heterogeneity of these coatings (mainly deposition defects), which can strongly modified the coating hardness. So, the indentation depths done at 200 nm of maximum penetration depth will not be taken into account along this section.

Comparing the results obtained and presented in this section with the ones in the bibliography, it can be said that they are in high concordance with Jiménez-Piqué results [4], as can be seen in the following graph:

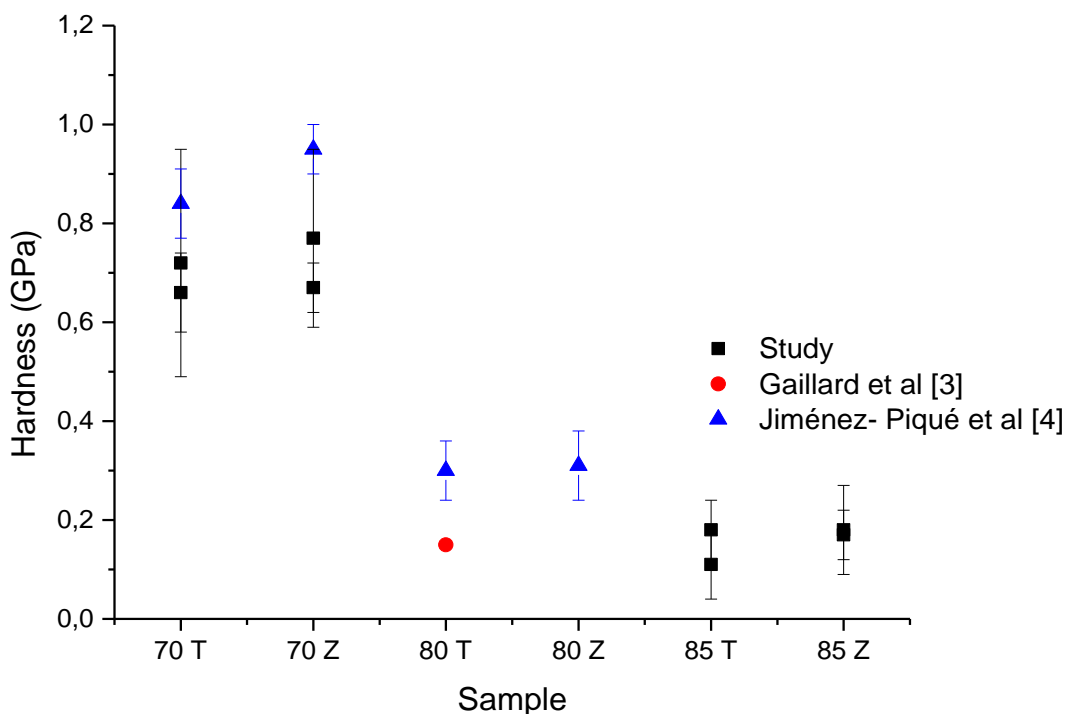


Figure 8.8.- Hardness comparison with bibliographic references.

8.1.2. Elastic modulus

In this section, the elastic modulus for each coating has been determined through two different experiments using two different types of indenter geometries, spherical and Berkovich and the different results supplied will be treated using the Hertz and the Oliver and Pharr equations, respectively (see **sections 4.3.1** and **4.4**).

8.1.2.1. Berkovich testing

The elastic modulus of each sample was extracted with the same process that was explained in **section 8.1.1**. In **¡Error! No se encuentra el origen de la referencia.** it can be appreciated the elastic modulus evolution along the $\text{TiO}_2\text{-SiO}_2$ coating against the displacement into surface.

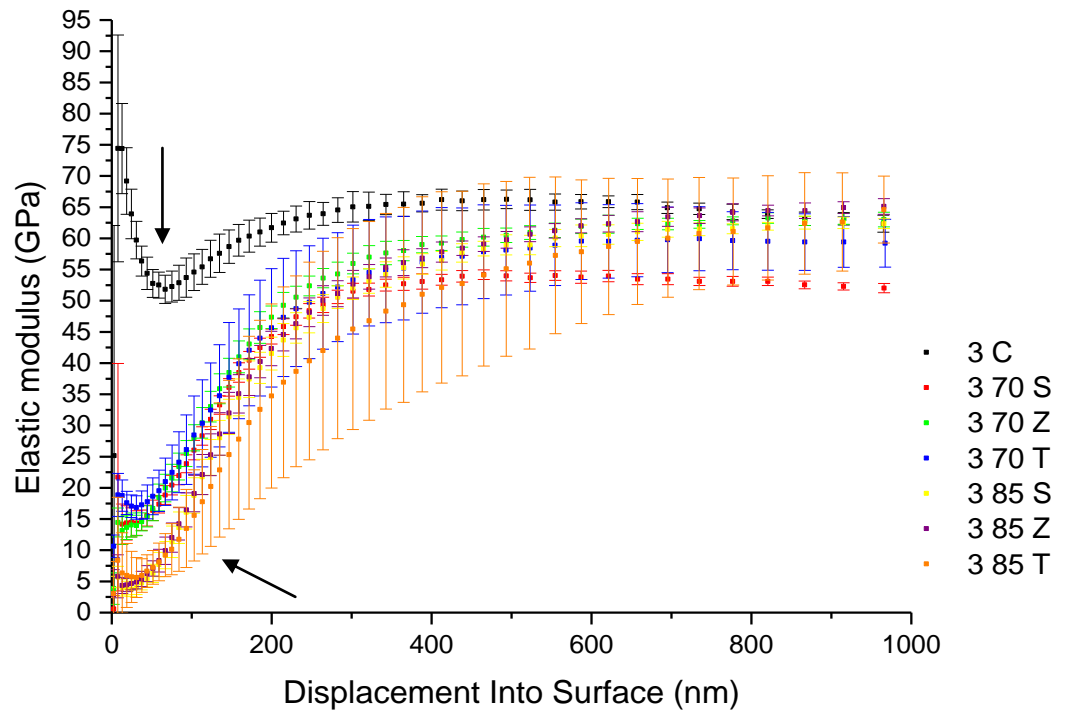


Figure 8.9.- Representation of the elastic modulus through the coating layer against the displacement into surface for the three layered samples.

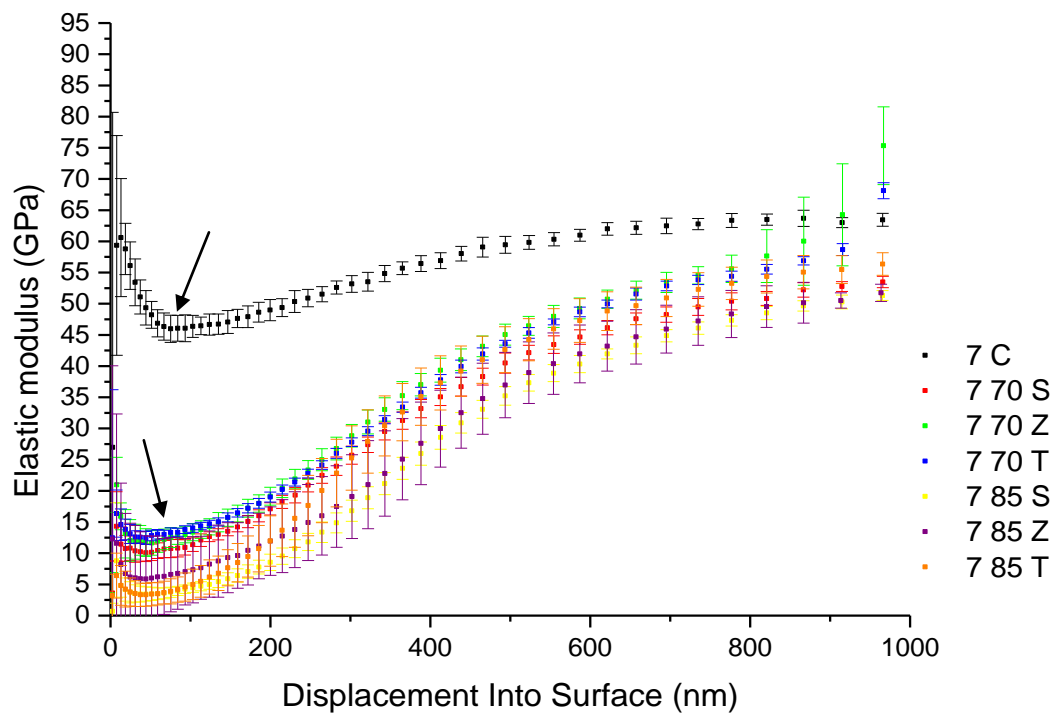


Figure 8.10.- Representation of the elastic modulus through the coating layer against the displacement into surface for the seven layered samples.

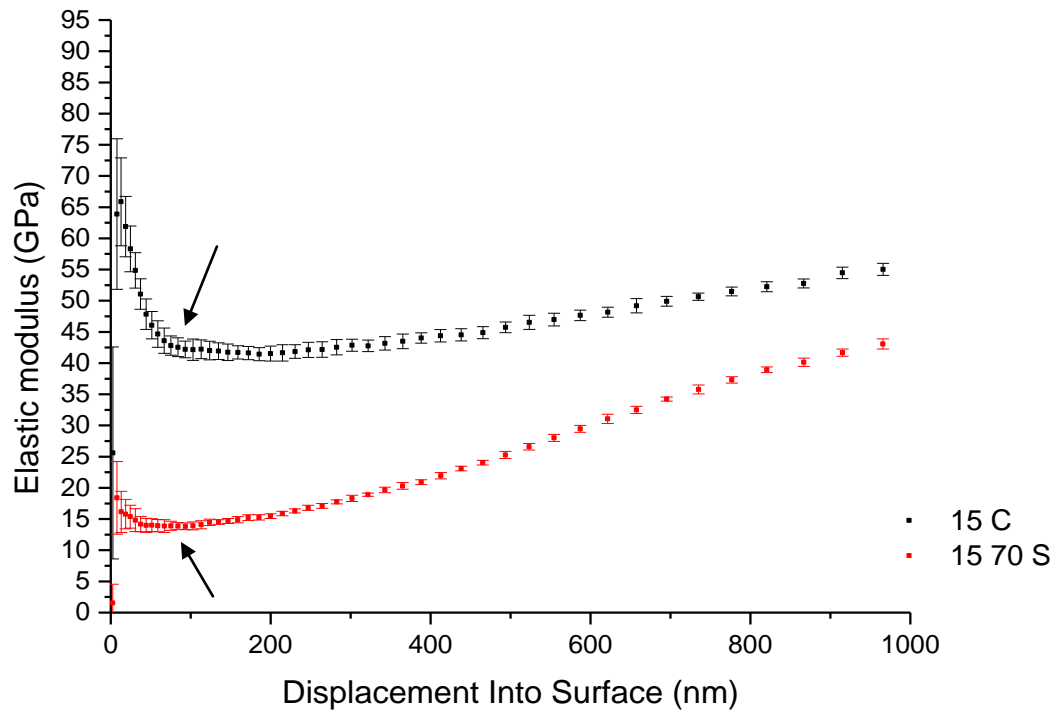


Figure 8.11.- Representation of the elastic modulus through the coating layer against the displacement into surface for the fifteen layered samples.

It can be seen that all the graphs present a little plateau in which they change their slope, which indicates that the elastic field induce during indentation starts to interact with the substrate, producing a considerable increase in this mechanical property because of the substrate of investigation is stiffer than the coating (see black arrows).

Figure 8.12 shows why the 1% rule can not be applied, due the elastic modulus was not correctly determined yielding a huge scattering between imprints or negative values as can be clearly seen. In this case it will be necessary to directly determine the coating elastic modulus using an analytical or empirical equation as commented in **section 4.4**. However, in this manuscript, the process used to extract the coating modulus was the extrapolation from the plateau until the beginning of the graph, as found in [33].

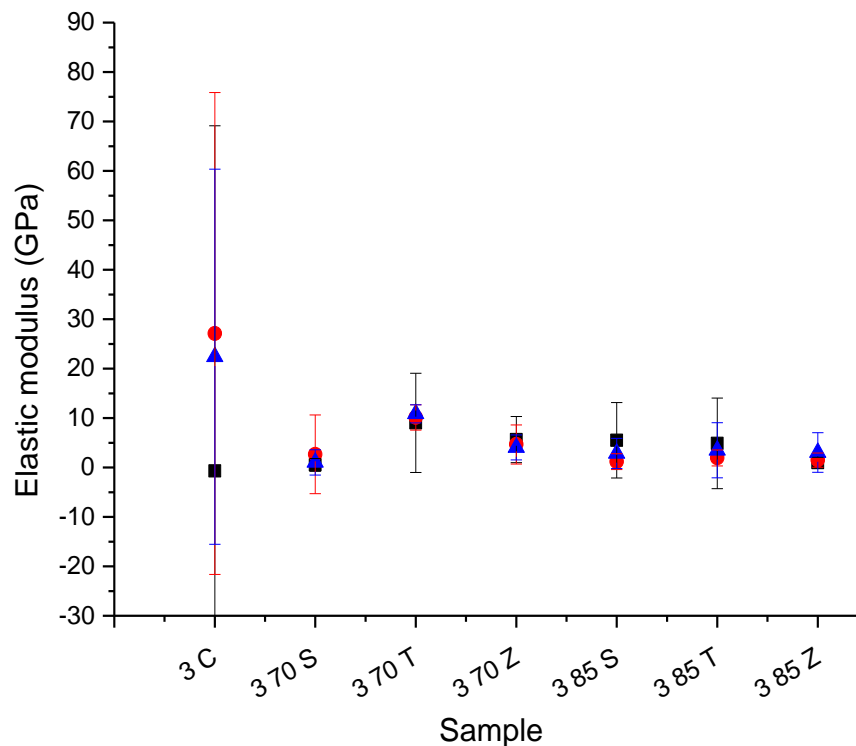


Figure 8.12.- Elastic modulus of the 3 layered samples. It can be seen that the 1% rule cannot be applied in this case. Black, red and blue marks correspond with the data obtained through imprints performed at 200, 500 and 1000 nm of maximum displacement into surface, respectively.

Three different groups have been made in order to organize the different values of the coating elastic modulus; **Compact**, which have the highest coating elastic modulus, around 48 ± 2 GPa, **70° samples**, which are the group of samples with a 70° growing angle and their coating elastic modulus is around 15 GPa; **85° samples**, which have the lowest coating modulus, rounding the 5 GPa.

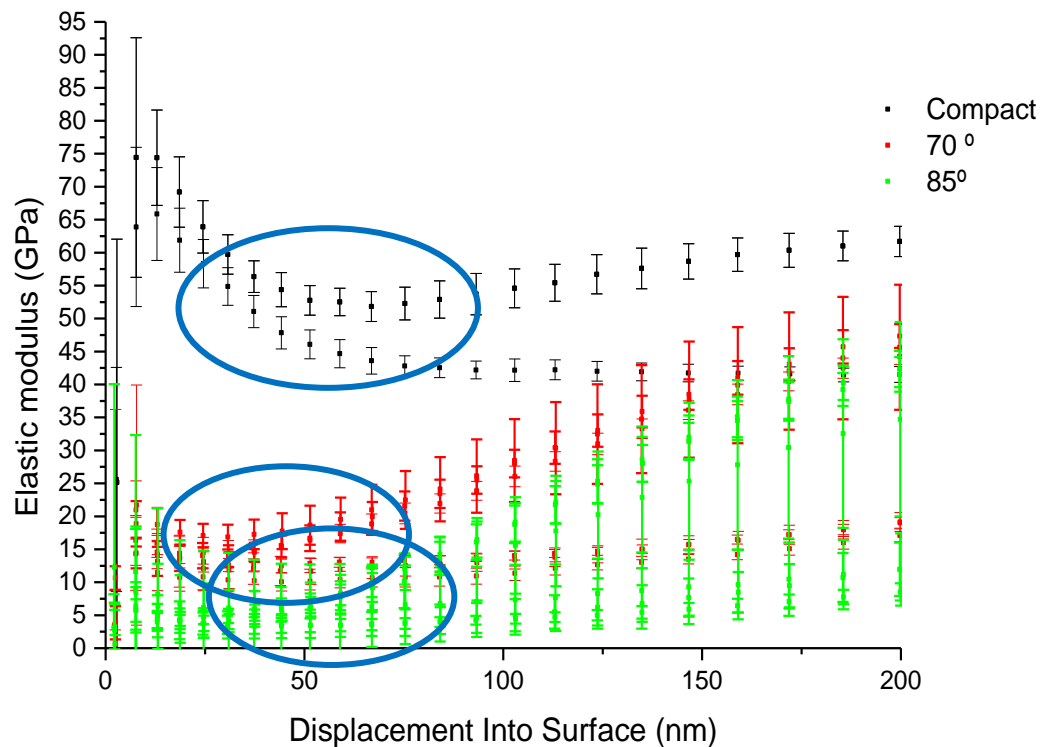


Figure 8.13.-Representation of the three different groups with the plateau highlighted

8.1.2.2. Spherical testing

In this section the elastic modulus determined from the Hertz equations by means of spherical tip indenter will be presented and compared with the values extracted with a sharp indenter and presented in the previous section. For that purpose, not all the samples were tested, in fact, the only group that was indented was the 7 70 group (the samples 7 C, 7 70 S, 7 70 Z and 7 70 T). The main reasons of not testing all the samples were: (i) the high amount of time to analyze the data acquired and (ii) as will be shown in the oncoming section, a relationship between the mechanical properties and the structure was not clearly seen for all the set of specimens tested in this project. However, a slightly correlation between the microstructure and the mechanical properties is appreciated for the 7 70 group, for this reason the spherical tests only have been done for these specimens in order to clearly observe a possible relation between microstructure and mechanical properties.

The data were treated using the Hertz equations as explained in **section 4.3.1**. Plotting the indentation load (P) against the penetration depth three half high ($h^{3/2}$) a linear part could be seen as it can be appreciated in **Figure 8.14** (see blue circle). Fitting the experimental data

to the Hertz equation, the effective elastic modulus can be determined from the slope of this fit and **equation 4.1**.

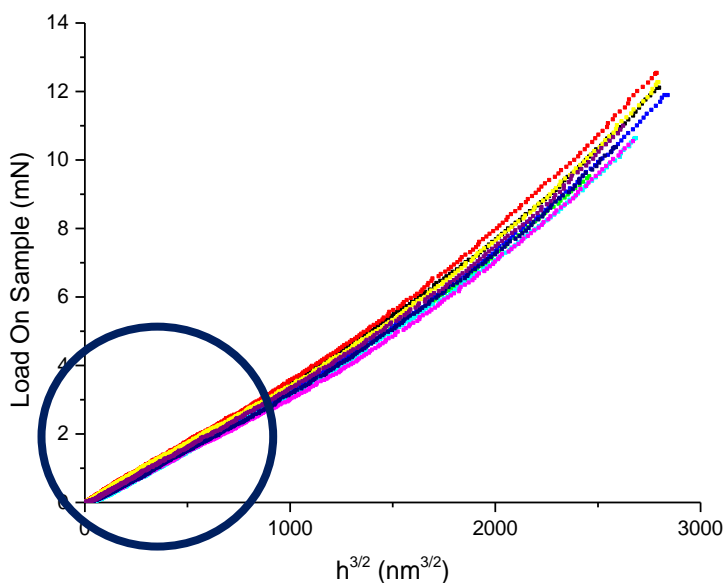


Figure 8.14.- Graph showing the nine different tests performed to 7 70 T sample.

All the elastic modulus found by spherical indentations were directly determined from fitting the experimental loading-unloading data until 1000 nm of maximum displacement into surface and using **Equation 4.1**. As it can be appreciated in **Table 8.2** and in **Figure 8.15**, the elastic modulus determined by means of spherical indentation is higher than the ones directly extracted from the Berkovich indentation.

Table 8.2.- Comparison between the two ways of extracting the coating elastic modulus.

Structure	$E_{\text{Berkovich}}$ (GPa)	$E_{\text{Spherical}}$ (GPa)	$E_{\text{Spherical}}/E_{\text{Berkovich}}$ (-)
C	48.1 ± 30.2	91.8 ± 3.1	1.9
S	11.0 ± 5.4	26.0 ± 1.5	2.4
T	15.1 ± 10.3	25.8 ± 1.8	1.7
Z	15.5 ± 4.1	32.3 ± 2.6	2.1

Where **C**: compact, **S**: spiral, **Z**: zig-zag and **T**: tilted.

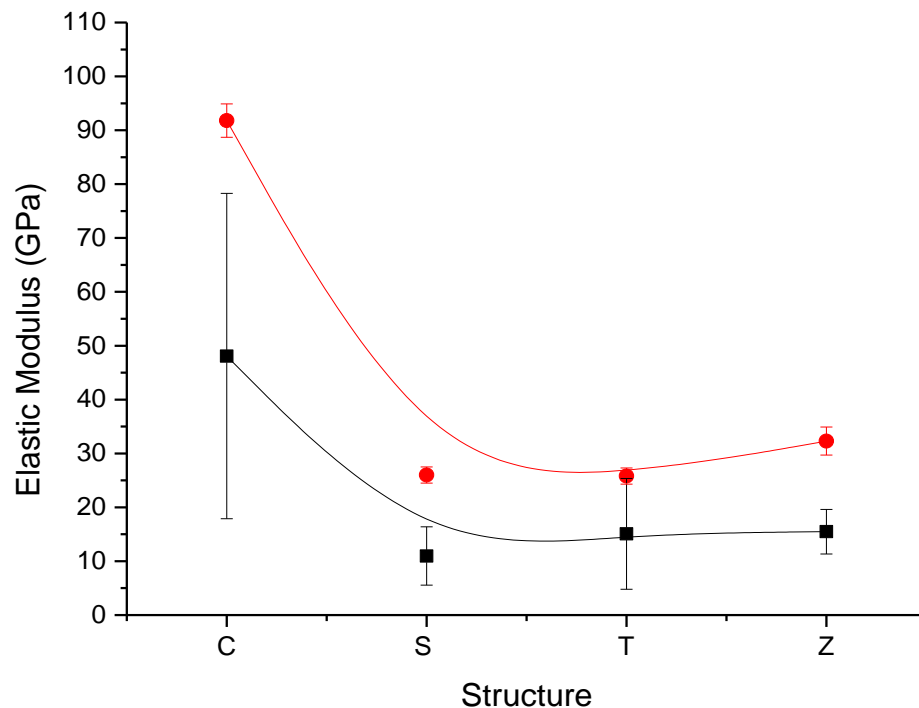


Figure 8.15.- Comparison between the two ways of extracting the elastic modulus. Red and black data corresponds with the elastic modulus determined using spherical and sharp tip geometries, respectively.

As it can be seen in the previous figure, the elastic modulus determined using blunt or sharp indenter follows the same trend, however the elastic modulus determined using a sharp tip indenter are slightly lower than the values determined using spherical indentation. This difference can be attributed to several factors: (i) the different ways to extract this mechanical property (to-zero extrapolation and/or the Hertz equation) and (ii) deformation and/or fracture events activated under different contact modes.

8.1.3. Indentation stress-strain curve

In this section the stress-strain curve (σ - ϵ) for the 770 samples will be presented, in order to understand how these coatings behaves under the first stages of plasticity as a function of the microstructure.

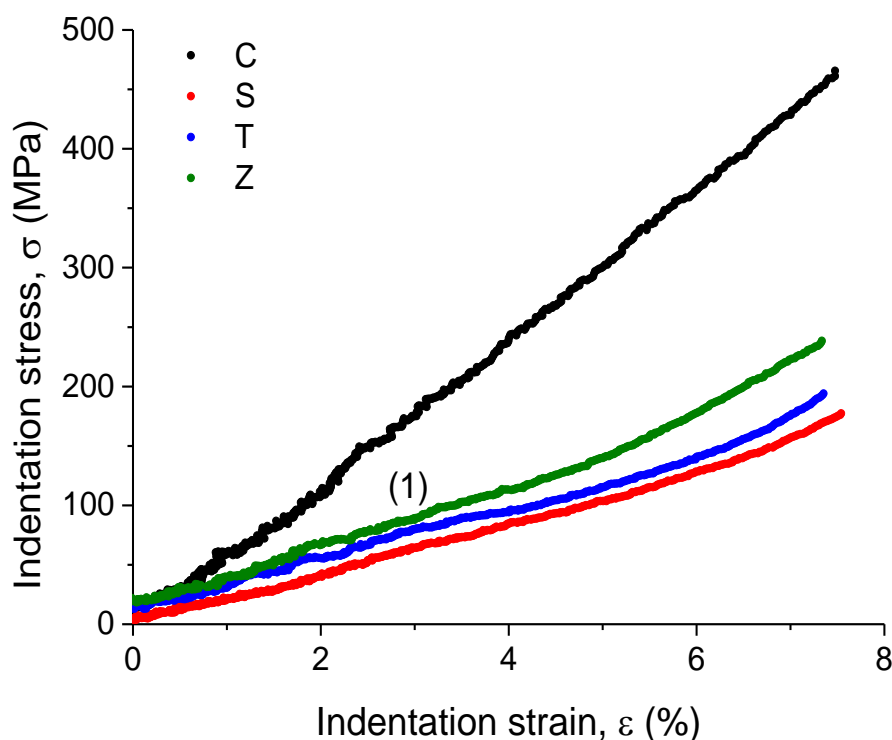


Figure 8.16.- Stress-strain comparison for the different structures studied in this project

In this figure only one experiment per condition has been represented in order to clearly distinguish and compare the stress-strain curve for each specimen investigated in this project. As it can be observed in **Figure 8.16**, two different trends can clearly be appreciated, one for the compact specimen and the other for the multilayered specimens with different coating geometries. This behavior may be attributed to the main deformation and/or fracture events induced in the coated layer during indentation process.

Furthermore, for the 7C sample, a linear trend can be observed. However, for the other three sets of specimens, three different regions can be clearly appreciated: (i) elastic trend for an indentation strain lower than 3%, (ii) reacomodation and/or densification process of the nanocolumns at an indentation strain of around 3% (labelled as 1 in this figure) and (iii) plastic deformation for strains higher than 3%.

Initially, the first region in the stress-strain curve can be related to the linear trend which corresponds with the elastic contact between the spherical indenter and the coating of interest. After certain stress (different for the T, S and Z specimen as depicted in **Table 8.3**) the stress-strain curve lose their lineality, denoted as (1) in this figure. Furthermore, this change in trend takes place around $\approx 3\%$, the same indentation strain for the S, T and Z

specimens. This phenomena may be attributed to a internal rearrangement and/or densification process of the coated layer. Attempting to corroborate this hypothesis and get more detailed view of the referred damage scenario, FIB cross-sections should be conducted in a future, see **section 8.3**. Finally, the last region in the indentation stress-strain curve could be interpreted as a plastic deformation of the TiO₂-SiO₂ coatings under the plastic deformation field induced during the indentation process.

Table 8.3.- Mean contact pressure where the rearrangement and/or densification process takes place for the specimens of study.

Specimen	C	S	T	Z
p_m (MPa)	Not appreciated	≈ 67	≈ 85	≈ 99

As it can be depicted in the previous table, the S specimens need less stress to produce the nanostructure rearrangement compared with the T and even the Z specimen. This results points out that the indentation stress-indentation strain is strongly dependent for multicoatings systems with complex microstructure.

8.1.4. Mechanical properties vs Microstructural properties

Graphics between the hardness and the microstructural properties have been made in order to determinate if there is any relationship between them. The following parameters were studied and compared:

- Structure: samples with the same growing angle and number of layers, changing the growing structure (S, T or Z).
- Angle: samples with the same number of layers and structure, changing the growing angle (70° or 85°).
- Number of layers: samples with the same structure and growing angle, changing the number of layers (3, 7 or 15).

This study was made only using the values determined at 500nm of maximum penetration depth, as can be seen in **Figure 8.7**, those values are similar to the 1000nm ones with less scattering associated.

8.1.4.1. Structure comparison

As it can be depicted in **Figure 8.17** all the specimens present a hardness value ranged between 200 up to 1000 MPa. Then, no clear tendency can be appreciated when the different deposition structures are compared. Two main reasons endure the lack of relationship: (i) in 7 70 samples the errors bars do not overlap and (ii) between 3 70 and 7 70

samples the hardness clearly decreases however, between 3 85 and 7 85 samples this reduction in hardness is not significant.

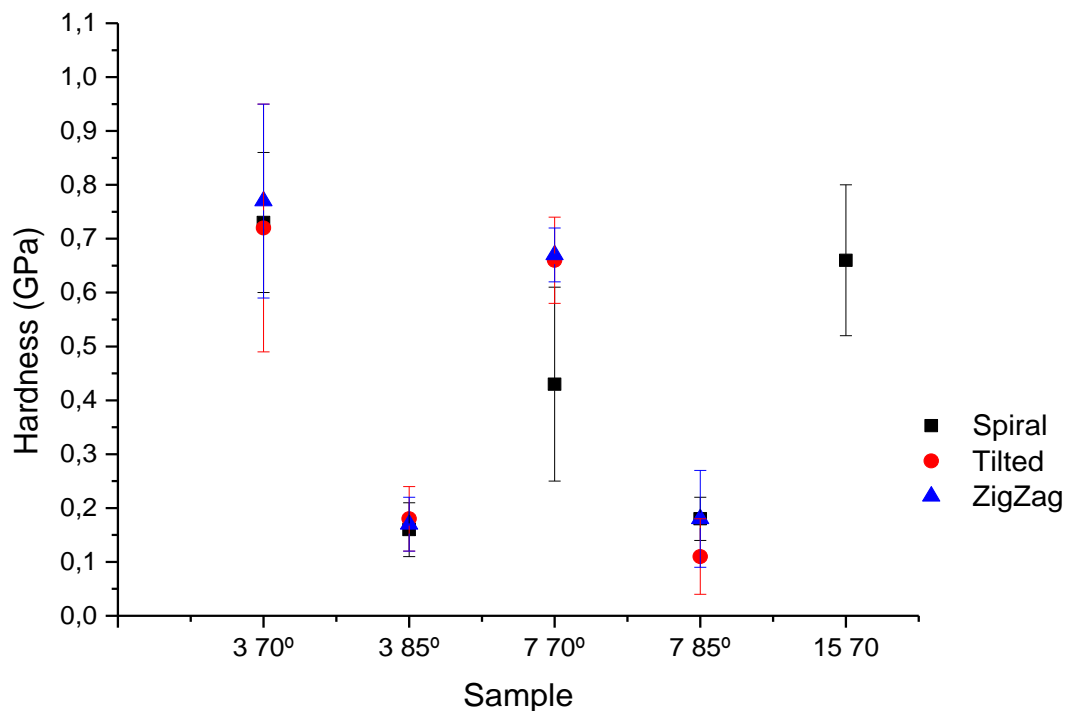


Figure 8.17.- Hardness vs structure representation.

8.1.4.2. Angle comparison

Figure 8.18 shows the dependence between the growth angle and the hardness for the different samples of study. The specimens with a titled angle of 70° are harder than the specimens with a misorientation of 85° . As it can be appreciated in this representation, as the angle increases, the hardness value decreases presenting a constant reduction of around 7%.

In order to compare different tests and, due the fact that its error has not much elevated, for this representation 500 nm and 100 nm penetration depth has been used.

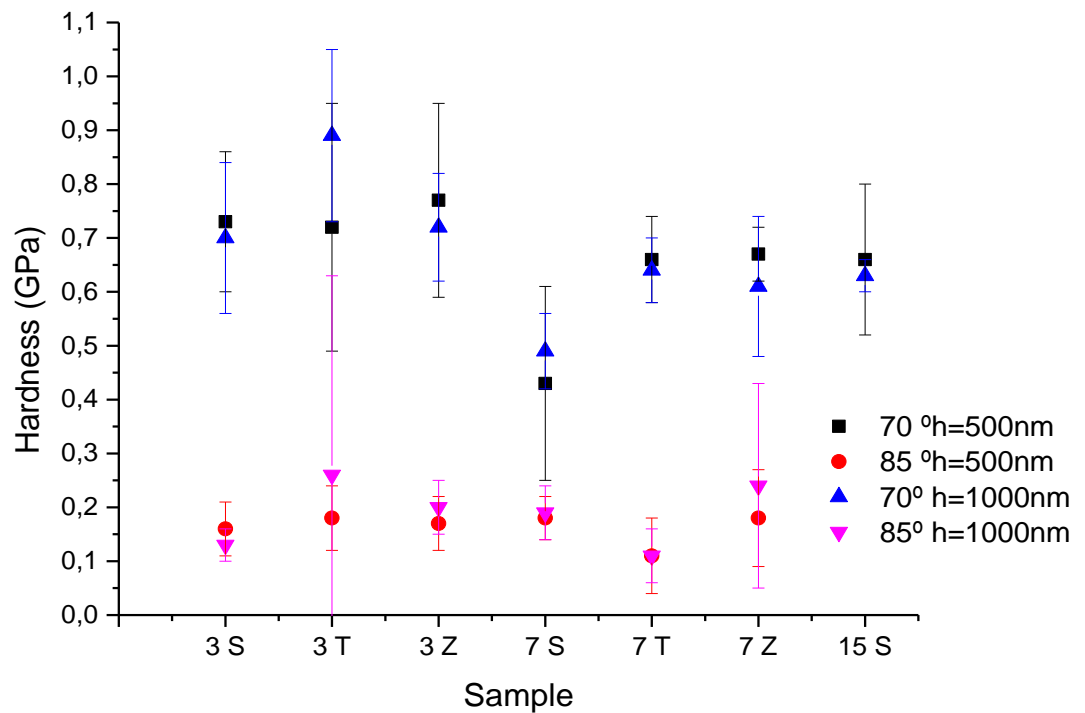


Figure 8.18.- Hardness vs angle representation.

8.1.4.3. Comparison by the number of layers

In **Figure 8.19** can be seen that the hardness does not depend on the number of layers that composes each sample because of the hardness value remains invariant.

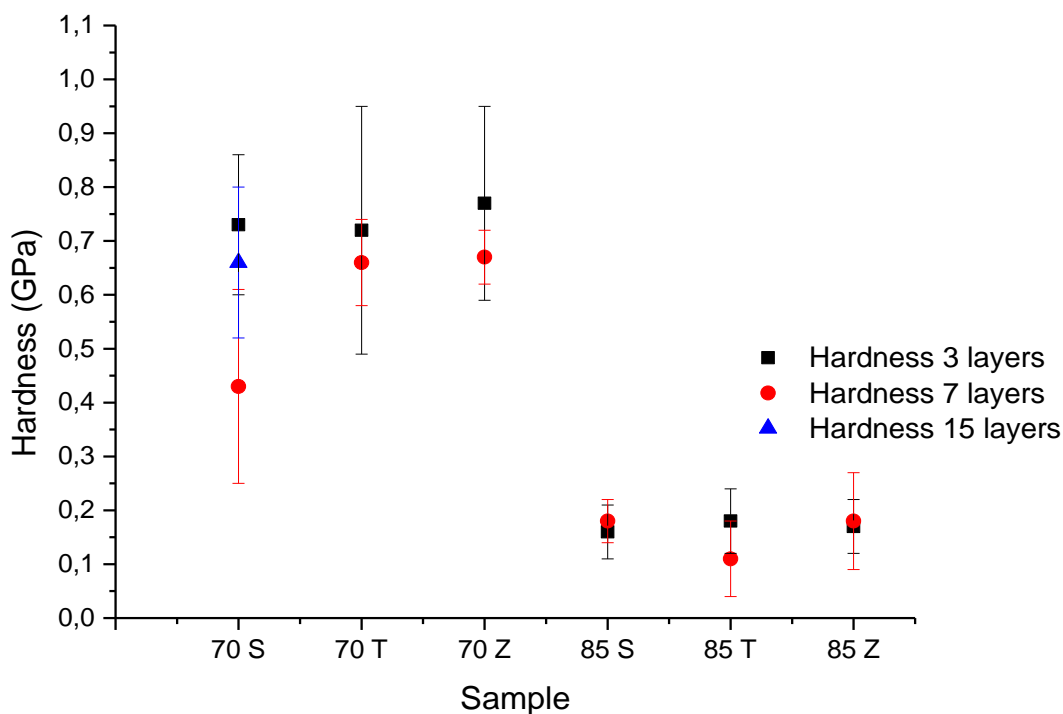


Figure 8.19.- Hardness vs number of layers representation.

After the hardness representation against several microstructural parameters it is possible to conclude that the main microstructural parameter which is slightly modified under indentation is the growing angle.

8.2. Fracture Events

In this section, the main fracture mechanisms activated under indentation as well as under sliding contact conditions will be pointed out.

Several fracture events were observed through the carefully observation of each residual imprint as well as each sliding track. All of them will be presented and described in detail below:

8.2.1. Chipping and pile-up damage effect

Chipping mostly occurs because of the generation of lateral crack parallel to the coating. Then, the locally stress field generated by a sharp tip produce a growing effect of these lateral cracks until reach the surface and the coating is chipped away from the surface, leaving a visible imprint in the apex. There are different chipping grades: massive or partial chipping (or denoted in this project as pile-up damage effect) as it depicted in the LSCM

images presented in **Figure 8.20** and **Figure 8.21**, respectively. The first case, all the coating has been removed and the residual imprint can be clearly observed in the substrate, while for the second case this fracture event denoted as partial chipping may be attributed to an interfacial decohesion. This is the first stage of fracture under indentation before appear the chipping effect. It is also necessary to highlight that for the 7 70 Z specimen (shown in **Figure 8.21**) the chipping effect is well delimited by a circumferential crack as it can be appreciated in the left hand side of this image.

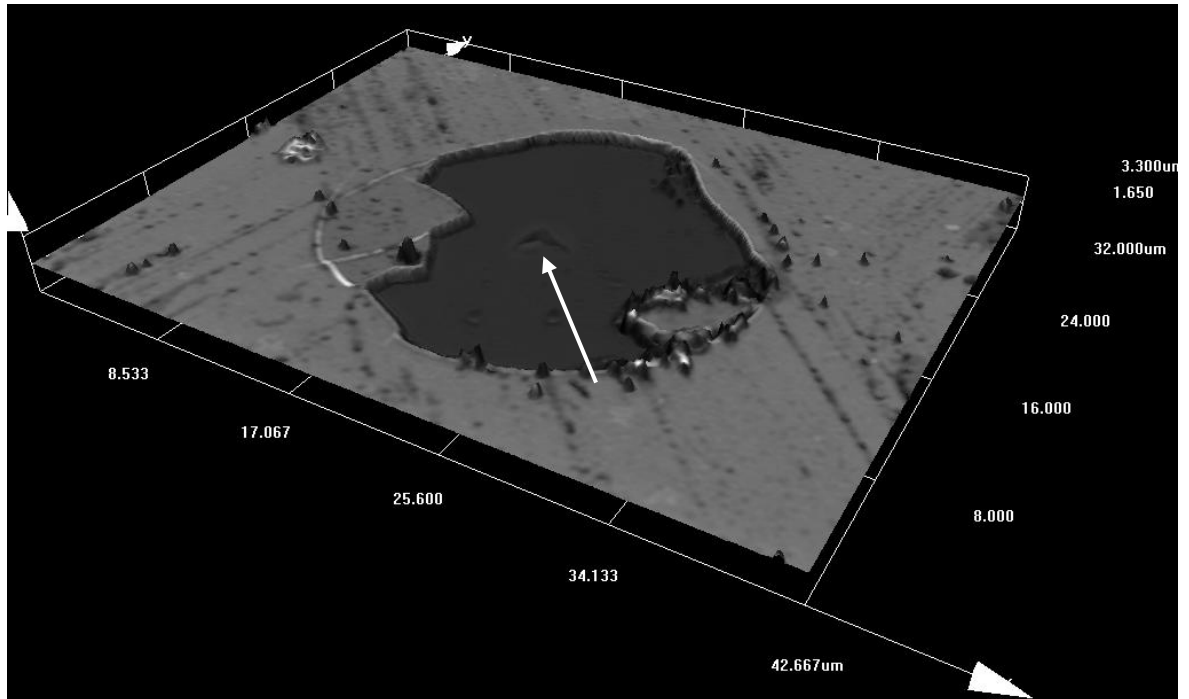


Figure 8.20.-LSCM picture of a residual imprint performed at 1000nm of maximum displacement into surface using a Berkovich tip indenter for the 3 C sample.

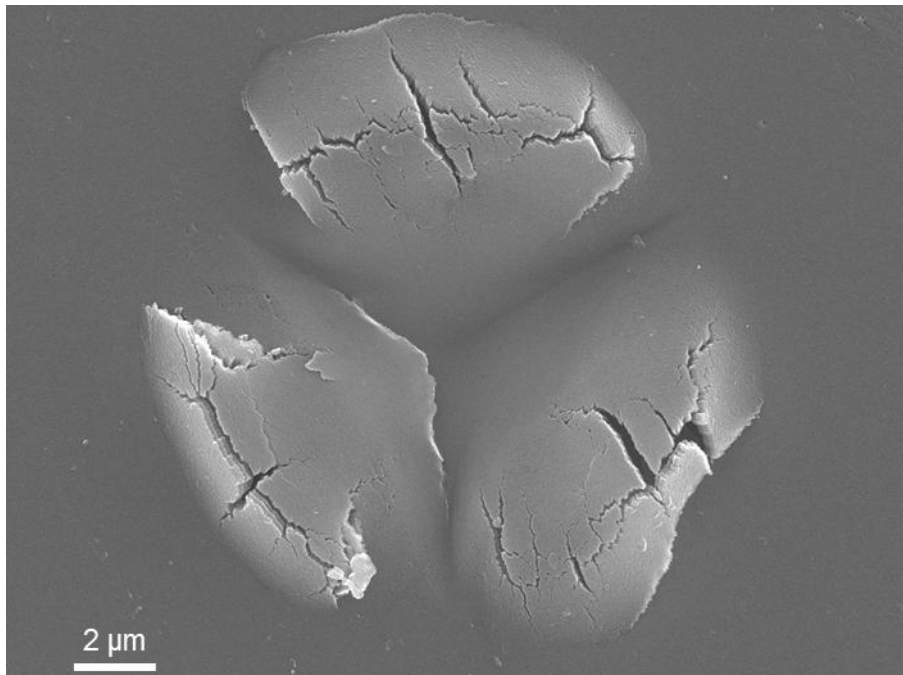


Figure 8.21.-FESEM image showing the main fracture mechanism for the 7 70 Z specimen.

8.2.2. Decohesion or interfacial cracking

Decohesion or interfacial cracking is defined as a crack growth direction with respect to the interfaces in the multilayer structures.

Such a fracture event should be studied using sub-superficial microscopes because of the superficial techniques like AFM it is not possible to clearly distinguish this fracture phenomena. **Figure 8.22** and **Figure 8.23** exhibit an AFM topographic image (3D-view) of a residual imprint done at 200 nm of maximum displacement into surface. No fracture events (i.e. radial cracks, chipping, etc.) are clearly depicted around or inside the residual imprint. However, the profile directly extracted from the topographic image, clearly shows a flat surface at the bottom of the residual imprint pointing out that it is possible that an interfacial cracking damage has been activated. Attempting to get more detail of this damage scenario, sub-superficial characterization is needed by means of FIB cross section, which will be presented in ongoing sections.

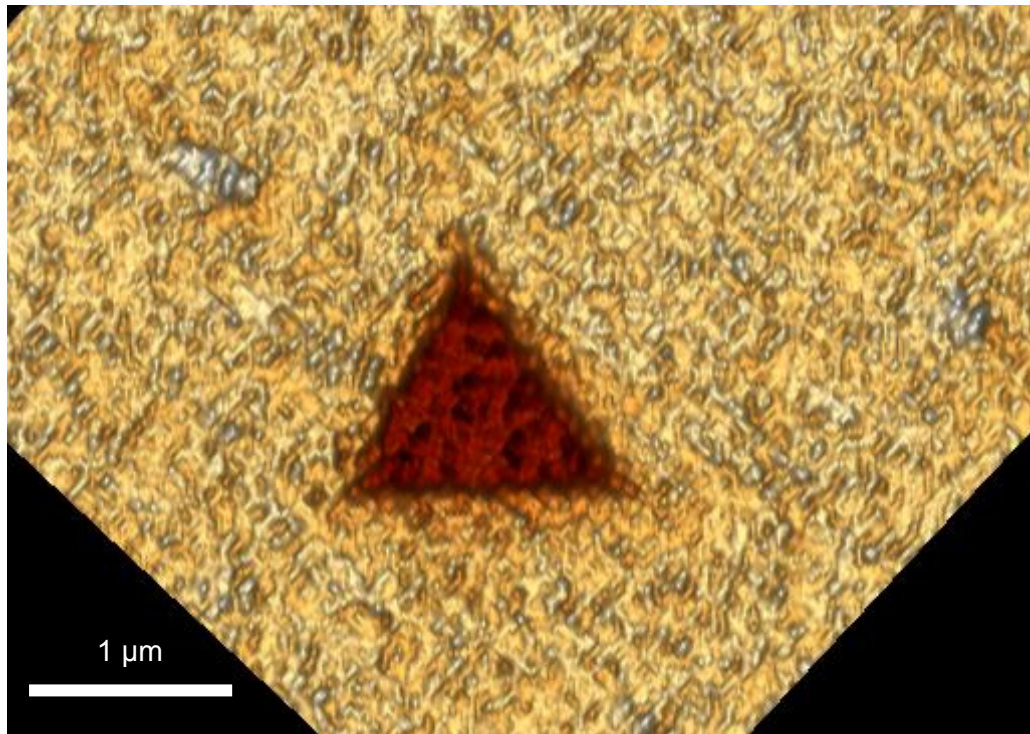


Figure 8.22.- Berkovich indentation at 200 nm performed into the 7 70 S sample. Topographic AFM image (3D view) where it can slightly appreciate interfacial cracking or decohesion between the multilayer coating and substrate.

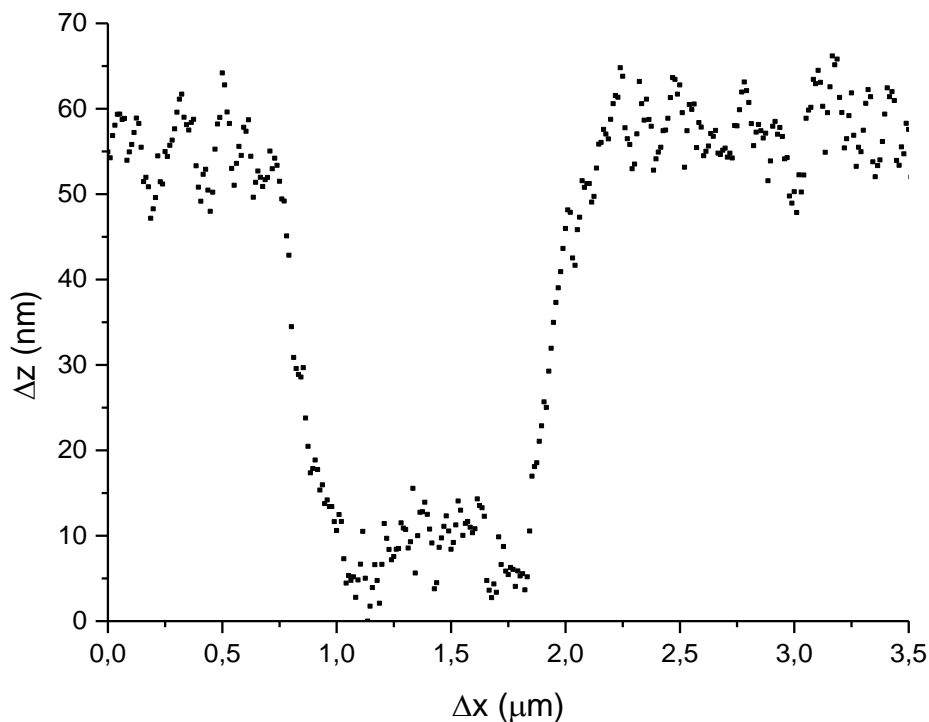


Figure 8.23.- Berkovich indentation at 200 nm performed into the 7 70 S sample. 2D profile directly obtained from the AFM image showing the shape of the residual imprint.

As it can be seen in the last images, neither chipping nor decohesion are similar in the different samples investigated here, due all of them present different microstructure. As the samples have an extremely orientated structure, it can be assumed that they should present some significant anisotropy.

In order to study this anisotropy of this set of samples (7 70 specimens), scratch testing was performed as explained in **section 7.2**.

8.2.3. Fracture events induce under sliding contact

The different scratches tracks present lots of different fracture mechanisms, all of them are compiled in ASTM 1624-05 standard [34].

The scratches tracks present lots of different fracture mechanisms [34], which it will be presented one by one below. The main damage events activated under sliding contact are: wedging spallation, spallation, chipping, chevron tensile cracks and buckling spallation, among others.

In most of the 85° and compact growth structure's samples, the fracture mechanism was based in a spallation process of the coating to the edges of the track, as can be seen in sample 3 C, see **Figure 8.24**. This is a general view point of the brittleness of this coating, due to coating does not maintain the mechanical integrity with the substrate.

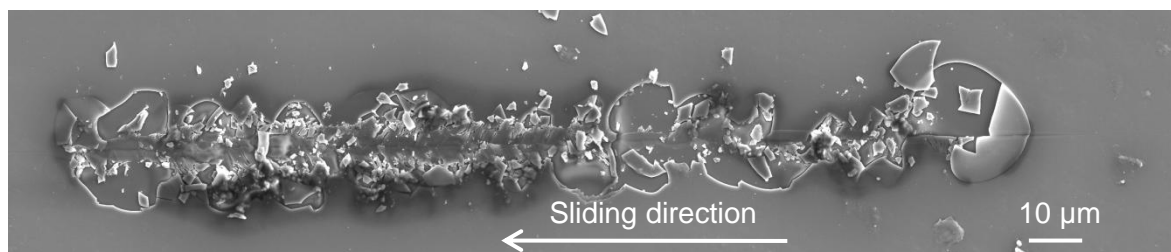


Figure 8.24- FESEM image presenting the general view of spallation process in 3 C sample. Scratch direction from right to left.

In **Figure 8.25** it can be appreciated two different fracture mechanisms activated at different loads, from left to right it can be observed: (i) chevron cracks inside the crack and (ii) spallation process due to an interfacial crack. The figure does not show any fracture inside the track, however at the edge of the crack where the field stress is maximum during the sliding process several radial cracks can be clearly discerned (see white dash circle). Also, when the load applied is higher than 78mN, these cracks situated at the edge of the track starts to growth until emerge into surface yielding another fracture mechanisms, spalling (see black dash circle) this phenomenon can be attributed to the generation of lateral cracks along the interface. Further sub-superficial inspection is necessary to corroborate this hypothesis.

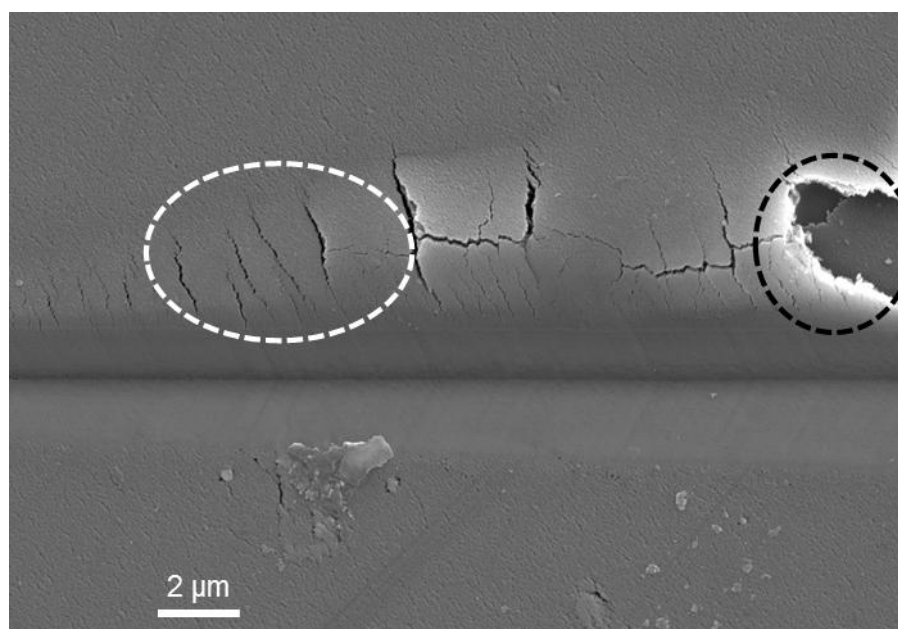


Figure 8.25.- FESEM micrograph for the 7 70 S sample, presenting Chevron cracks (white dash circle) and spallation (black dash circle).

In **Figure 8.26** it can be clearly appreciated some radial cracks at the track edge as well as some decohesion phenomena on the 15 70 S sample. This kind of decohesion effect is similar at the one seen under indentation process for the 7 70 S specimen in **Figure 8.22a**. Also, the main fracture mechanisms activated in this picture are similar than the damage observed and commented previously in **Figure 8.25**.

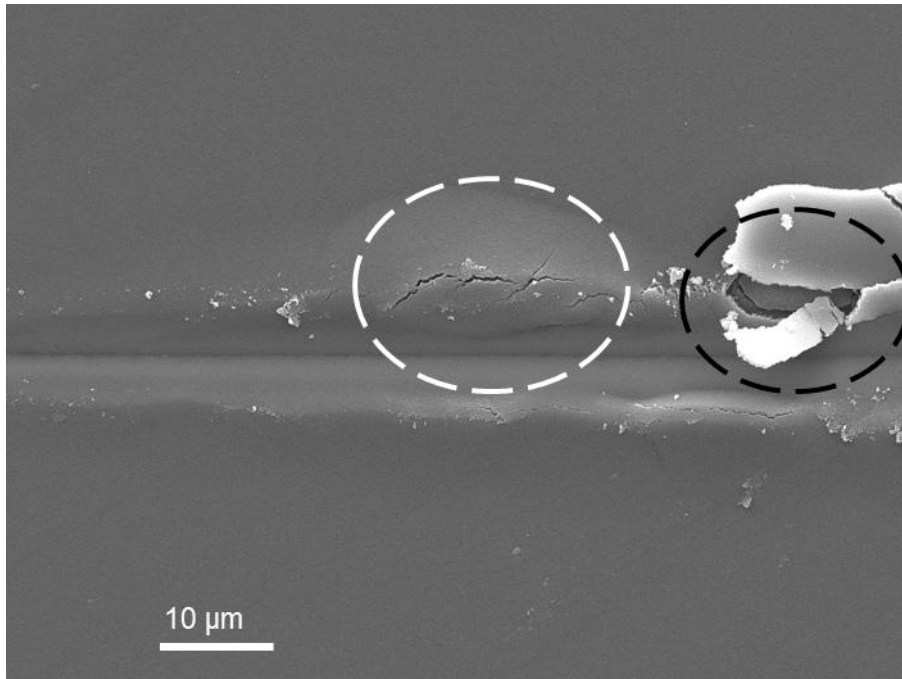


Figure 8.26.- FESEM image presenting several fracture events activated under sliding contact: radial cracking (white dash circle) and decohesion (black dash circle) occurred in 15 70 S sample.

Finally, the initial part of the sliding track for the 3 85 T sample (see **Figure 8.27**), it can clearly be seen no fracture events during the initial micrometer, after that some spalling is clearly appreciated at the track edge.

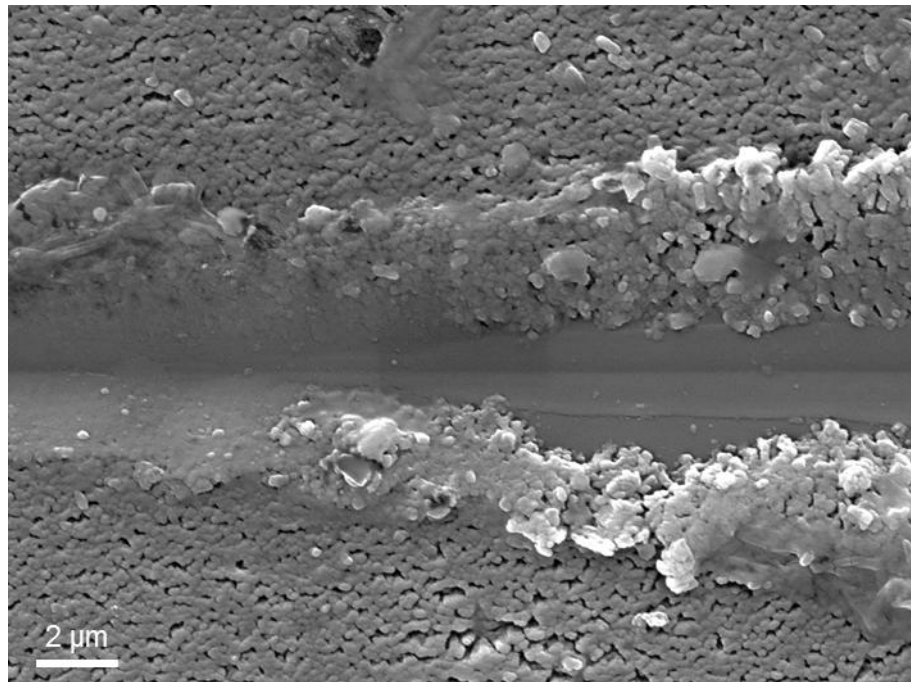


Figure 8.27.- FESEM image showing the initial track for the 3 85 S sample.

After this superficial observation for the sliding tracks by FESEM it is necessary to perform some sub-superficial observations in order to clarify which is the main responsible to induce chevron cracks, decohesion or even spalling under this contact mode.

8.3. Sub-superficial observation

FIB cross sectioning was done for the 7 70 specimens. **Figure 8.28** shows a general view from the nanoscratch track performed at 150 mN of applied load for all the different set of 7 70 samples with different microstructure, pointing out that all the deformation induced during the sliding process is confined inside the coating and the substrate has not been plastically deformed. As it can be appreciated in **Figure 8.28**, all specimens present an interfacial decohesion. This mode of cracking is a commonly experienced failure mechanism in coated systems, where cracks can nucleate from stress concentrations at the edge of layered structures. For the C specimen, some microcracks parallel and perpendicular to the interlayer can be clearly observed in **Figure 8.28a**. However, for the S and Z specimens (**Figure 8.28b** and **Figure 8.28d**, respectively), an interfacial cracking between two successive layers are clearly observed as well as in some cases perpendicular to the layer interface due to the stress concentration. Finally, the T specimen (see **Figure 8.28c**), presents less fracture than the other specimens due to the layer microstructure helps to absorb the plastic deformation induced during the sliding contact as well as this specimens presents the best substrate/coating adhesion. However, as it can be clearly appreciated in

the left hand side of this image a distortion of the different multilayers can be clearly observed mainly attributed to the stress field induce during the sliding process.

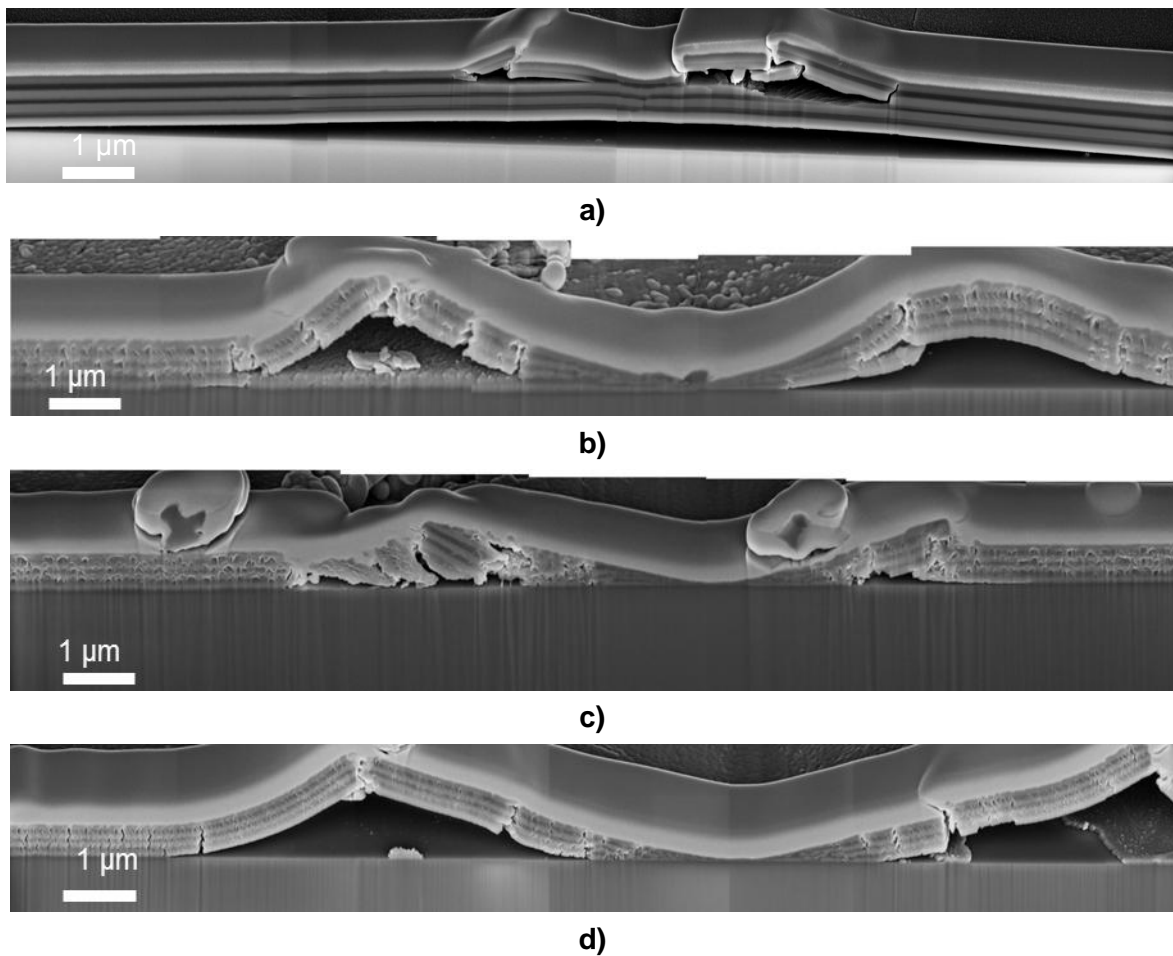


Figure 8.28.- Sub-superficial damage for the 7 70 specimens with different coating geometries: **a) C**, **b) S**, **c) T** and **d) Z**.

The sample 7 85 S was also observed with FIB/FESEM in the sliding track corresponding with an applied load of ~ 150 mN in order to compare the damage produced in the 70° samples with different deposition angle (85°), see **Figure 8.28b** and **Figure 8.29**, respectively. For this specimen, no decohesion mechanisms are visible in this image pointing out that this deposition angle does not produce decohesion due to the coating surrounding the sliding track maintain the mechanical integrity. However, as it can be slightly appreciated in this image, in this region the indenter will be in contact and deform plastically the substrate and delaminate the coating. It is important to highlight that the damage scenario for this coating is located around the sliding track and no damage events are appreciated far from the nanoscratch track as was clearly observed for the set of specimens previously shown, 7 70.

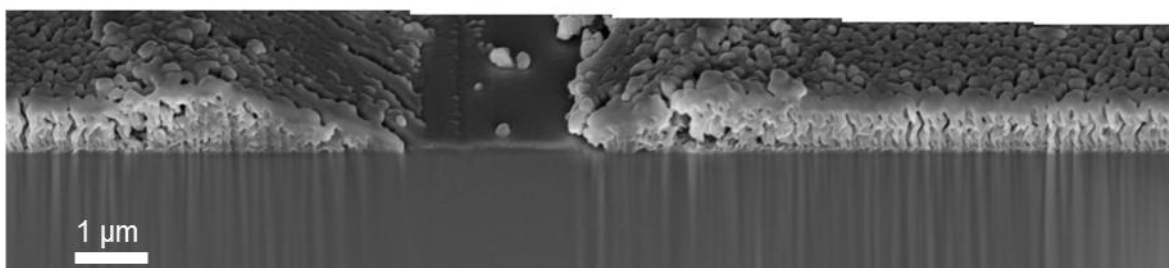


Figure 8.29.- Sub-superficial damage in 7 85 S sample.

The main sub-superficial damage seen in the last two figures can be summed up in **table 8.5** and presented in the oncoming figures:

Table 8.4.- Fracture mechanisms for each sample studied and the mark used to highlight them in **Figure 8.30**.

Fracture mechanism / Sample	7 C	7 70 S	7 70 T	7 70 Z	7 85 S	Mark
Coating-Substrate delamination	X	X		X	X	Blue
Coating decohesion		X		X		White
Coating compaction		X	X	X		Black
Layers rotation			X		X	Green
Layers breaking	X					Red
Fracture through layers	X					Orange

In **Figure 8.30** all the different samples stitching and its fracture mechanisms highlighted using a dashed circle colored as explained in the last column of **Table 8.4** can be seen:

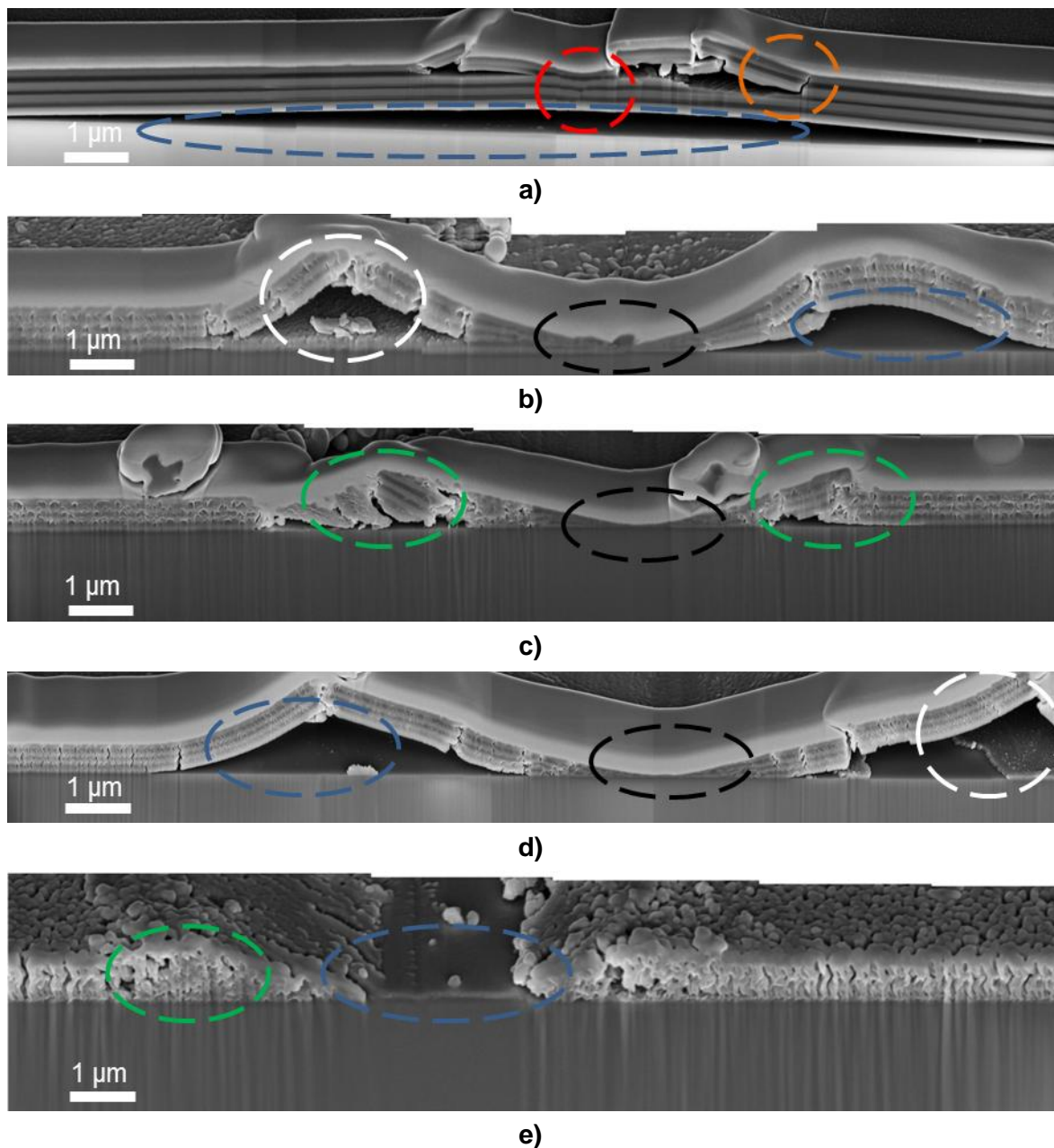


Figure 8.30.- Different fracture mechanisms highlighted in different samples: **a)** 7 C, **b)** 7 70 S, **c)** 7 70 T, **d)** 7 70 Z and **e)** 7 85 S.

In the following lines all the fracture mechanisms previously observed are going to be described in detail:

- **Delamination between the substrate and the coating**

In this fracture any junction between both parts can be seen, so it is easy to think that the adherence of the coating is not the optimum. This kind of fracture could have been minimized or even avoided by using a porous substrate. This mechanism was seen in 7 C, 7 70 S and 7

70 Z samples. It also was seen in 7 85 S, but that kind of delamination does not present any fracture mechanisms, while the 70° presented cracking in the interface.

- **Coating decohesion**

This fracture event takes is located in the coating, where two different coating layers loose contact between them. This event has been observed for the 7 70 S and Z specimens, where the initial layer of TiO₂ remained attached to the substrate.

- **Coating compaction**

In the center of the sliding track, the stress field generated during the sliding process by the indenter was the responsible of the compaction of the coating. The highlighted part (marked with a black circle) it is thought that the layers had rotated upon themselves, increasing the layer thickness on both sides. However, no explanation about why this mechanism takes places is found along the literature.

- **Layers rotation**

The coating layers had rotated due the scratch test and, during this process, the delamination between the coating and substrate was observed, as can be seen in the 7 70 T and 7 85 S, see **Figure 8.30e** and **Figure 8.30d**, respectively.

- **Layer breaking**

It can be seen in the left part of **Figure 8.30a**, which corresponds to 7 C sample, and it was caused by the pressure of the indenter added to the fact that the coating was compact, without having any chances to dissipate energy creating parallel cracks to the surface, yielding a reduction of their mechanical integrity.

- **Fracture through layers**

The pressure exercised on the track center was dissipated breaking the layer's continuity and creating some fractures that go through the layers and, when a weak point was found, the fracture was able to move up to others layers.

8.4. Tribological characterization

Using the FESEM images presented in **section 0** (see **Figure 8.32**) it is possible to directly determine the critical loads for each sets of specimens investigated in this project. The following graph sums up all the critical length results obtained from the tribological characterization explained at **section 4.5**.

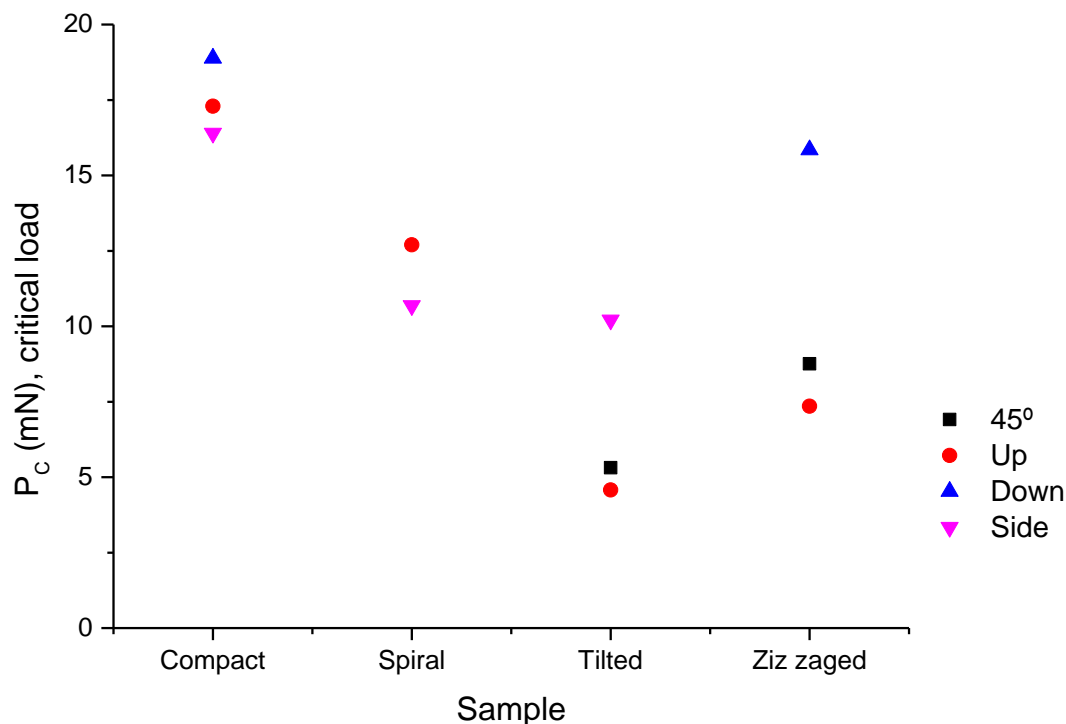


Figure 8.31.- Critical load for each sample and direction investigated.

As can be seen in the previous figure, the highest critical load corresponds to the compact specimen, which at the same time is strongly isotropic due to the different critical load does not depends with the scratch direction. However, the critical load for the spiraled coating is slightly different (~ 4%) being the up direction slightly stronger than the side direction. Then, it can be considered that the spiral coatings are isotropic as the compact coatings. The tilted and zig-zaged coatings present similar trend, being the critical load for the up direction the lowest one. For these specimens, the sliding direction is really important being the side and down direction the strongest one for the tilted and zig-zaged structure, respectively.

As a summary, for the tilted and zig-zaged coatings had a preferential orientation that made them to have different mechanical responses depending on where they are measured. It can

also be seen that, if the preferential orientation is taken out, there is a relationship between the critical load P_C and the coating structure.

Next, stitching of all the samples in direction UP is shown:

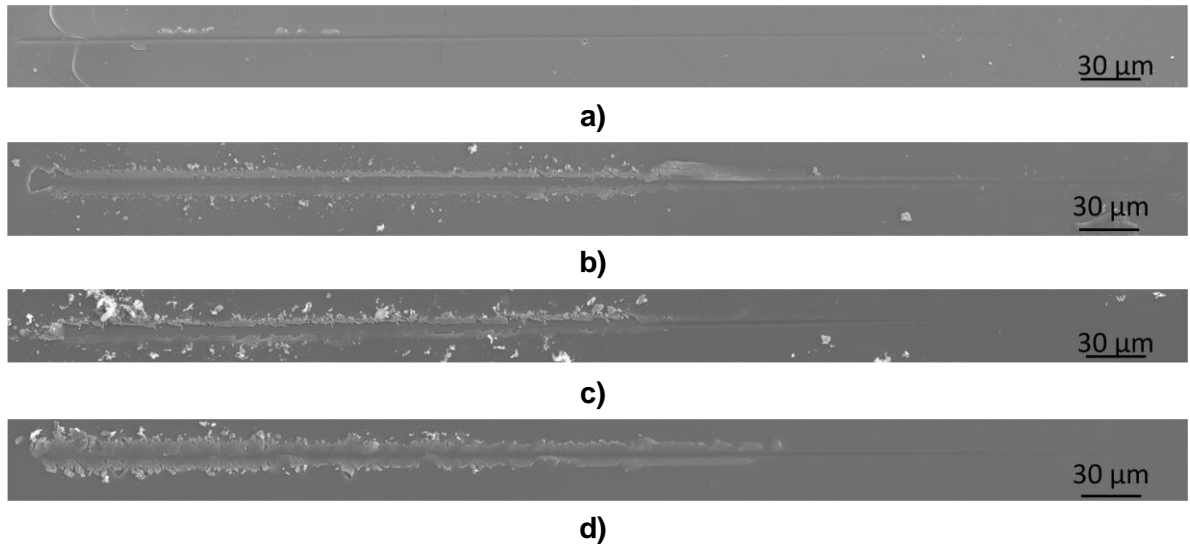


Figure 8.32.- Stitching of the different samples scratched in DOWN direction: **a)** 7 C, **b)** 7 70 S, **c)** 7 70 T and **d)** 7 70 Z

As can be seen, the type and the presence of damage along the track present big differences depending on the coating structure. While the compact sample, **Figure 8.32a**, starts to present some decohesion in the last micrometers of the track, the tilted and zigzagged one presents radials cracks in the first quarter of the track ($\approx 125 \mu\text{m}$). The spiraled sample presents decohesion in the middle of the experiment.

9. Conclusions

i) Mechanical vs structural properties:

The hardness is inverse to the growing angle (70° or 85°), and does not show a strong dependency with the number of layers of the coating. It is also clear that there is a relation between the mechanical properties and the microstructure of the coating (C, S, Z or T), and there is no relationship between the mechanical properties and the number of layers that form the coating.

ii) Cohesive and adhesive damage

The damage under scratching is strongly anisotropic for the tilted and zig-zaged samples (T and Z), whereas it is strongly isotropic for the compact and spiraled specimens (C and S). Then, the coating microstructure mainly governs the main damage located in the coating/substrate interface activated under different contact loads because of the lack of adherence between the coating and the substrate.

iii) Fracture events

Depending on the coating microstructure (C, T, Z and S), the fracture events are completely different. Mainly, some lateral cracks growing parallel to the $\text{TiO}_2/\text{SiO}_2$ interface as well as layer rotation are clearly visible through the coating under different contact scenarios.

10. Future Work

In the indentation test filed, two main things could have been done:

- For a first estimation, using the 10% and to-zero extrapolation in order to extract the mechanical properties does not create a much error, but the use parametric and analytic models should have reduced that error and obtain an accurate parameter for each coating investigated.
- To use a DCM tip indenter instead of the XP used in this project, will help to perform the mechanical characterization at lower penetration depth due to the indenter tip used in the DCM head is sharper than the Berkovich tip used in the XP head.

In order to minimize the decohesion of the coating, the substrate could be changed for a more porous one which would hold the coating better, and the mechanical properties of the ensemble would be increased.

11. Environmental Impact

Any kind of solid waste was generated during this project, due all the tests performed, although they chipped the samples, the volume chipped was in the order on micrometers. The same explanation can be said for the volumes milled using FIB microscope. Due any kind of polishing was needed, no type of liquid waste was generated.

In order to use all the equipment, such as the nanoindenter or all the microscopes, energy was required and, greater accuracy mean greater energy consume, while LSCM only needed to be connected to the electrical monophasic net, FESEM or FIB needed triphasic electricity connection. All this electrical consume had its generation costs and its environmental impact whereas nuclear wastes or CO₂ send to the atmosphere, that cannot be negligible, and can be rated as 330g CO₂/KWh_e consumed [35].

12. Economical Study

The economic cost of this work has been split in two different groups; personnel and machines and consumables and it has been distributed as can be seen in the following **Table** with the final cost of **44.898 €**.

Table 12.1.- Costs center of the work

Group	Item	Cost	Hours (h) / Units (u)	Total (€)
Personnel	Junior Engineer	20 €/h	1440 h	28800 €
	Director	60 €/h	90 h	5400 €
	Laboratory technician	40 €/h	100 h	4000 €
	Subtotal			38200 €
Machines and consumables	Nanoindenter	40 €/h	52 h	2080 €
	LSCM	40 €/h	56 h	2240 €
	AFM	50 €/h	24 h	1200 €
	AFM probe	18 €/unit	1 unit	18 €
	FESEM	35 €/h	16 h	560 €
	FIB/FESEM	50 €/h	12 h	600 €
	Subtotal			6698 €
Total				44898 €

13. Acknowledgments

All this work could not have been done without the help and guidance of Dr. Emilio Jiménez-Piqué and Dr. Joan Josep Roa, who taught me in all the necessary and helped with the writing. I would like to thank them for sharing all their knowledge and also for all the fun during the project, as the long sessions of AFM enlivened by cheating each other in *Worms*. Also for the help and patience shown by Dr. Roa with the text, sum up with the more than 4.000 comments made during the 12 drafts that have been written. By the way, after the thesis defense we will enjoy with a precious beer☺.

I want also to thank *Centre d'Integritat Estructural i Fiabilitat dels Materials*, CIEFMA and his director, prof. Dr. Anglada for the access facility to their installations and, in particular, to Francesc Heredero, who taught and helped me with all the LSCM issues.

Also to *Centre de Recerca en Nanoenginyeria*, CRnE, with special attention to Trifon Trifonov for his knowledge of the center and help with FIB.

References

- [1] Pinho, L.; Elhaddad, F.; Facio, D.; Mosquera, M. "A novel TiO₂-SiO₂ nanocomposite converts a very friable stone into a self-cleaning building material". *Applied Surface Science*, vol. 275 (2013), p. 389– 396
- [2] Kapridaki, C.; Maravelaki-Kalaitzaki, P. "TiO₂-SiO₂-PDMS nano-composite hydrophobic coating with self-cleaning properties for marble protection". *Progress in Organic Coatings*, vol. 76 (2013), p. 400– 410
- [3] Gaillard, Y.; Rico, V.J; Jiménez-Piqué, E.; González-Elipe, A.R. "Nanoindentation of TiO₂ thin films with different microstructures". *Journal of Physics*, vol.42 (2009), p. 1-9
- [4] Jiménez-Piqué, E., González-García, L.; Rico, V.J.; González-Elipe, A.R. "Nanoindentation of nanocolumnar TiO₂ thin films with single and stacked zig-zag layers". *Thin Solid Films*, vol. 550 (2014), p. 444-449
- [5] Center for Materials and Devices for Information Technology Research: *Physical Vapor Deposition PVD - Vacuum/thermal coater* [Accessed: February 2014]. [online]. Available in: <http://photonicswiki.org/index.php>.
- [6] Zhao, Y.P.; Yeb, D.X.; Wangb, C.G.; Lub, T.M. "Designing Nanostructures by Glancing Angle Deposition". *Proceedings of SPIE*, vol. 5219 (2003), p. 59-74
- [7] Oliver, W.C. Pharr G.M. "An improve technique for determining hardness and elastic modulus using load and displacement sensing indentation experiments". *Journal of Materials Research*, vol. 7 (1992),p. 1564-1583
- [8] Beegan, D.; Laugier, M.T. "Application of composite hardness models to copper thin film hardness measurement". *Surface and Coatings Technology*, vol. 199 (2005),p. 32-37
- [9] Fischer-Cripps, A.C. *The IBIS Handbook of nanoindentation*. Forestville: Fischer-Cripps Laboratories Pty Ltd, 2009. ISBN 0 9585525 4 1

- [10] VanLandingham, M.R. "Review of Instrumented Indentation". *Journal of Research of the National Institute of Standards and Technology*, vol. 108 (2003), p. 249-265
- [11] Field, J.S. ; Swain, M.V. "A simple predictive model for spherical indentation of materials". *Journal of Material Research* vol. 8 (1993), p. 297-306
- [12] Hertz, H. "On the contact of elastic solids". *Math*, vol. 92 (1881), p. 156-171. (Translated and reprinted in English in Hertz's Miscellaneous Papers, Macmillan and Co., London (1986) Chapter 5).
- [13] Jiménez-Piqué, E.; Galliard, Y.; Anglada, M. "Instrumented indentation of layered ceramic materials". *Key Engineering Materials*, vol. 333 (2007), p. 107-116
- [14] Hay, J.; Agee, P.; Herbert, E. "Continuous stiffness measurement during instrumented indentation testing". *Experimental Techniques*, vol. 34 (2010), p. 86-95.
- [15] ROA ROVIRA, Joan Josep. PhD thesis. "Mechanical properties of HTSC at micro/nanometric Scale". Directors: Mercè Segarra Rubí and Javier Garcia Capdebila. Universitat de Barcelona, Department of Materials Science and Metallurgical Engineering, 2010
- [16] Fischer-Cripps, A.C. *Nanoindentation*. 2nd ed. New York: Springer, 2004
- [17] Fischer-Cripps, A.C. "Critical review of analysis and interpretation of nanoindentation test data". *Surface & Coatings Technology*, vol. 200 (2006), p. 4153 – 4165
- [18] Oliver, W.C.; Pharr, G.M. "Measurement of hardness and elastic modulus by instrumented indentation: Advances in understanding and refinements of the methodology". *Journal of Material Research*, vol. 19 (2004), p. 3-20
- [19] Tuck, J.R.; Korsunsky, A.M.; Bull, S.J.; Davidson, R.I.; "On the application of the work-of-indentation approach to depth-sensing indentation experiments in coated systems". *Surface and Coatings Technology*, vol. 137 (2001), p. 137-217

- [20] Bec, S.; Tonck, A.; Loubet, J.L. "A simple guide to determine elastic properties of films on substrate from nanoindentation experiments". *Philosophical Magazine & Philosophical Magazine Letters*, vol. 86 (2006), p. 33-35
- [21] Saha, R.; Nix, W.D. "Effects of the substrate on the determination of thin film mechanical properties by nanoindentation". *Acta Materialia*, vol. 50 (2002), p. 23-38
- [22] Rar, A.; Song, H.; Pharr, G.M. "Assessment of new relation for the elastic compliance of a film-substrate system". *Material Research Society Symposium*, vol. 695 (2002), p. 431-438
- [23] Jäger, I.L. "Comment on: Effects of the substrate on the determination of thin films mechanical properties by nanoindentation, by Saha and Nix". *Scripta Materialia*, vol. 47 (2003) p. 429-432
- [24] CSM Instruments SA. *CSM scratch testers: nano, micro and nano range*. Switzerland, 2006.
- [25] Oliva-Ramírez, M.; González-García, L.; Parra-Barranco, J.; Yubero, F.; Barranco, A.; González-Elipé, A.R. "Liquids Analysis with Optofluidic Bragg Microcavities". *ACS Applied Materials Interfaces*, vol. 5 (2013), p. 6743–6750
- [26] Olympus. *Confocal Scanning Laser Microscope LEXT OLS3100/OLS3000 User's manual*. 5th ed. Japan, 2007
- [27] Swapp, S. *Integrating Research and Education-moving research into geoscience courses-SEM*[Online] Wyoming, 2012.[Accessed July 2014]. Available: http://serc.carleton.edu/research_education/geochemsheets/techniques/SEM.html.
- [28] Yao, H.; Kimura, K. "Field Emission Scanning Electron Microscopy for Structural Characterization of 3D Gold Nanoparticle Superlattices". *Modern Research and Educational Topics in Microscopy*, vol. 2 (2007), p. 568-576
- [29] Wilson, R.; Bullen, H.A. ,Tutorial "Introduction to Scanning Probe Microscopy (SPM)-Basic Theory - Atomic Force Microscopy (AFM)". University, Highland Heights: Northern Kentucky University, 2006.

- [30] Horcas, I. et al. "WSxM: A software for Scanning Probe Microscopy and a Tool for Nanotechnology". *Nanotechnology Review of Scientific Instruments*, vol. 78 (2007), p. 2677-2692
- [31] Brucherseifer, M. *SEM/ FIB* [Online]. Brucherseifer, M. 2010 [Accessed July 2014]. Available: http://www.brucherseifer.com/html/sem_fib.html
- [32] Carpenter, R. *Knock Atoms Off by FIB* [Online]. Carpenter, R., October 2010. [Accessed July 2014]. Available: <http://handchat-castle3-euig7arc.blogspot.com.es/2012/10/contributor-r-carpenter-knock-atoms-off.html>
- [33] ISO 14557-3: 2002. *Metallic materials, Instrumented indentation test for hardness and material parameters. Part 4: Test method for metallic and non-metallic coatings.*
- [34] ASTM C 1624-05. *Standard Test Method for Adhesion Strength and Mechanical Failure Modes of Ceramic Coatings by Quantitative Single Point Scratch Testing.*
- [35] International Energy Agency (IEA) "World Energy Outlook 2012". *International Energy Agency Publications*, vol. 1 (2012) p. 49-80.